Civil Engineering and Applied Solutions

Research Article

journal homepage: ceas.journals.umz.ac.ir

Evaluation of the Static Behavior of WPC-GFRP Sandwich Panels: An Experimental, Theoretical, and Numerical Study

Amin Norouzi [a], Morteza Naghipour [a*]

[a] *Faculty of Civil Engineering, Babol Noshirvani University of Technology, Babol, Iran*

A R T I C L E I N F O

Keywords:
Wood plastic composite (WPC)
Glass fiber-reinforced polymer (GFRP)
Static behavior
Sandwich panels
Finite element method (FEM)

Article history:
Received 26 July 2022
Accepted 31 October 2022
Available online 9 November 2022

A B S T R A C T

Wood-plastic composite (WPC) is a material composed of wood particles, recycled plastics, and resin, and plays an important role from an economic standpoint. Due to its high compressive and tensile strength, WPC can be used as decking in applications such as pier flooring or small bridge decks. In this study, different glass fiber-reinforced polymer (GFRP) layers were employed to investigate the ultimate load, stiffness, and maximum deformation of WPC-GFRP sandwich panels. Given WPC's lower tensile strength relative to its compressive strength, the reinforcing layers were primarily applied to the bottom face sheets. The loading applied in these experiments was of two types, linear and point loading, perpendicular to the panel surface, to simulate the conditions when such panels are used as flooring. Following the experimental program, theoretical and numerical methods were employed for further analysis of the specimens. In the theoretical approach, beam theory was used because the loading, support conditions, and material behavior closely resembled those of beams. In the numerical approach, uniaxial tests were conducted to determine the material properties and stress–strain relationships, which were then implemented in the finite element model. Overall, the results indicate that the use of a single GFRP layer significantly improves both the strength and stiffness of the panels. However, adding multiple layers does not lead to a considerable improvement in strength, although it slightly enhances stiffness. From an economic perspective, the use of more than one GFRP layer does not appear to be cost-effective. Furthermore, a good agreement was observed among the experimental, theoretical, and numerical results, confirming the reliability of the modeling approaches.

1. Introduction

With the rapid increase in global population and the corresponding surge in industrial and infrastructural demands, the need for a wide range of advanced materials has become increasingly critical. Among these, composite materials have emerged as a pivotal solution, offering enhanced performance through the combination of two or more distinct constituents. Composites, by definition, are multi-phase materials whose overall properties surpass the individual contributions of each constituent, creating synergistic effects that improve stiffness, strength, and durability. Such characteristics make composites suitable for a broad spectrum of engineering applications, including aerospace, automotive, naval structures, sports equipment, bridges, and buildings. The efficient utilization of composite materials requires a precise understanding of their mechanical, thermal, and durability characteristics, as well as the implementation of design strategies tailored to their unique behaviors. Wood-plastic is a new composite that has been used in countries around the world and in our country in the last few years. The superior properties of this material compared to its constituent materials (wood and plastic) have led to the increasing use of this material in industry. Its main advantages include the use of recycled wood and plastic waste in its production [1-6]. These materials have been used in different forms over time. The

---

* Corresponding author.
E-mail addresses: m-naghi@nit.ac.ir (M. Naghipour).

https://doi.org/10.22080/ceas.2025.30123.1044

How to cite this article: Norouzi, A., Naghipour, M. Evaluation of the Static Behavior of WPC-GFRP Sandwich Panels: An Experimental, Theoretical, and Numerical Study. Civil Engineering and Applied Solutions. 2026; 2(2): 1–27. doi:10.22080/ceas.2025.30123.1044.

value and importance of these materials in different societies have varied over time.

The term wood-plastic composites refers to composites that are made of wood in any form and plastics in both thermoset and thermoplastic forms. A product made from a combination of wood and thermoplastics (thermosets) is known as a wood-plastic composite, from which a wide variety of products are obtained for use in various industries. Thermosets (thermosets) are plastics that, once processed, cannot be melted again by heating. These materials, which include resins such as epoxies and phenolics, are in fact plastics that closely resemble industrial forest products (wood) [5]. Wood-plastic composites are the result of combining wood and plastic, where the skill in combining these two components has resulted in the emergence of excellent joint properties. They inherit the hardness and strength of wood and plastic, but their density is often higher than both. The properties of these materials are derived directly from their structure; that is, they are an internal combination of wood and plastic elements [7].

Among composites, wood-plastic composites (WPCs) have gained prominence due to their ability to integrate recycled wood fibers and plastic polymers, thus offering both environmental and structural benefits. The modern concept of WPCs emerged in Italy in the 1970s, and production was initiated by the American company Woodstock in 1783. North American adoption accelerated in the early 1990s, followed by expansion into Asia, including India, Malaysia, Singapore, Japan, and China in the early 21st century. Reports indicate a production increase from 460 million tons in 1999 to approximately 700 million tons by 2001, with annual growth rates of around 18% in North America and 14% in Europe [8]. Plastics must have high ultimate strength and stiffness and exhibit high resistance to fracture. This means that although the plastic has a desirable stiffness, it does not undergo brittle fracture. It should also be noted that if a composite is to be subjected to tensile loading, in order to achieve all the mechanical properties expected from the combination of fibers and plastic, a plastic that is at least as flexible and deformable as the fibers must be selected. The reason for the greater use of plastics is that they have desirable mechanical properties at a reasonable cost. Thermoplastic materials are viscoelastic. This means that their mechanical properties are a product of the behavior of elastic liquids and solids. Therefore, when a thermoplastic material is subjected to stress, the material responds by both dissipating energy in the form of viscous flow and storing energy in the form of elastic displacement. The properties of a viscoelastic material depend on time, temperature, and the rate of strain application. However, conventional stress-strain testing is used to investigate the short-term mechanical properties of plastics [9]. WPCs exhibit superior moisture resistance, absorbing only ~0.7% water compared to ~17.2% in pine wood, thereby significantly reducing susceptibility to fungal attack and decay. These materials can be further engineered by selecting specific wood species and polymers, enabling tailored mechanical and thermal properties suitable for diverse industrial and structural applications. In addition to the effective use of wood and plastic waste, they have significant advantages such as resistance to moisture, mold, and insects, long-term durability, and low maintenance [10-13]. These properties have led to WPCs being widely used in decks, flooring, railings, doors and windows, and decorative components [14]. Despite these advantages, the main limitation of WPC is its relatively low strength and stiffness compared to traditional materials such as concrete, steel, or natural wood [15]. For this reason, the widespread structural use of WPCs is challenging, especially in components that require high load-bearing capacity or high flexural and shear performance. This has led researchers to strengthen WPCs using more advanced materials.

Fiber-reinforced polymers (FRPs) are composite materials that combine high-strength fibers, such as carbon, glass, or aramid, within a polymeric matrix. FRPs were first employed in Europe and Japan during the 1980s for retrofitting concrete structures, replacing corroded steel plates, and reducing installation complexities [16-18]. The fiber phase provides primary tensile strength and stiffness, with typical aspect ratios exceeding 1000, while the polymer matrix ensures load transfer, environmental protection, and durability [18]. Placement, orientation, and volume fraction of fibers critically influence flexural, tensile, compressive, and fatigue performance, as well as thermal and electrical properties.

Experimental investigations have demonstrated the effectiveness of FRP reinforcement for timber and composite structures. Triantafillou Thanasis and Deskovic [13] proposed analytical models for stress-strain behavior of timber members reinforced with FRP sheets, revealing significant improvements in stiffness and load-bearing capacity. Li et al. [11] analyzed CFRP-reinforced timber beams under four-point bending, documenting notable enhancements in flexural resistance and reductions in midspan deflection. Furthermore, Naghipour et al. [14] evaluated the damping characteristics of multilayer glulam beams reinforced with GFRP, indicating up to 40% increases in stiffness and load resistance.

Sandwich panel systems, comprising two stiff faces separated by a lightweight core, offer high rigidity with minimal weight. Originally conceptualized by Delau in 1820, sandwich panels were extensively applied during World War II in aircraft structures, such as the Mosquito, where material shortages necessitated lightweight, high-strength solutions. Early core materials included soft plastics like polystyrene and polyurethane; subsequent development introduced higher-density, stiffer polymers, allowing for broader civil and industrial applications. The integration of WPC and FRP in sandwich panels yields high structural performance, including exceptional resistance to moisture, decay, and mechanical loading. For instance, WPC PVC has successfully supported industrial dock decks under forklift wheel loads distributing 1600-lb per wheel, demonstrating considerable structural reliability [19, 20]. Despite these positive findings, a review of the literature shows that comprehensive and systematic research on the static behavior of WPC-FRP panels is very limited. Many of the existing studies have either only investigated simple WPC beams and slabs or have focused only on the strengthening of concrete and timber members with FRP. There is a significant research gap in the field of investigating the complete static behavior of WPC-FRP sandwich panels, including load capacity, stiffness, deformations, and failure mechanisms.

Nonlinear analytical models, including those proposed by Naghipour et al. [4], have effectively predicted the flexural behavior of WPC-FRP reinforced structures, incorporating exponential stress-strain relationships and accounting for both elastic and plastic responses under load. Such models are essential for accurate prediction of load-displacement behavior, structural safety, and durability under real-world conditions.

Although several studies have examined the mechanical and flexural behavior of WPC or FRP-reinforced timber members, most previous investigations have focused on individual aspects such as the tensile or flexural performance of WPC beams [3, 9, 14–16] or the strengthening of timber members using external FRP sheets [13, 14]. Very few studies have systematically evaluated the combined behavior of WPC-FRP sandwich panels under realistic loading conditions. Furthermore, previous research has often been limited by: (1) the absence of integrated experimental, theoretical, and numerical evaluation, leading to uncertainties in model validation; (2) simplified material assumptions, where nonlinear and asymmetric tension compression behavior of WPC was not fully represented; and (3) insufficient attention to the failure mechanisms, such as shear or debonding between face sheets and the WPC core.

These limitations have restricted the structural application of WPC-FRP systems in flooring and decking components. Therefore, there remains a clear research gap in developing a comprehensive understanding of the static performance, stiffness, load capacity, and failure mechanisms of WPC-FRP sandwich panels. The present study addresses these gaps by performing a combined experimental, theoretical, and finite-element analysis to assess the flexural behavior of WPC-GFRP sandwich panels, offering insights that can guide the design of lightweight and sustainable structural systems.

Despite these advancements, critical gaps remain in understanding long-term performance, microstructural behavior, and optimization of fiber-matrix combinations in sandwich and composite structures. Addressing these gaps is vital for the design and implementation of high-performance composites in civil, industrial, and marine applications. This study aims to comprehensively evaluate WPC-FRP sandwich structures, investigating their mechanical behavior, durability, and practical applications, thereby contributing to the optimization of composite design and reinforcing strategies in contemporary engineering contexts.

2. Research significance

Wood-plastic composite represents a relatively new class of composite materials that has garnered increasing attention due to its unique combination of mechanical performance, durability, and sustainability. While WPC has been widely applied in non-structural components, such as decking, furniture, and decorative elements, its potential for use in primary structural applications, including bridge decks, small-scale flooring, and load-bearing panels, remains largely unexplored. Understanding and optimizing the mechanical properties of WPC for structural use is therefore of significant importance, as it can lead to the development of lightweight, durable, and cost-effective structural members. The significance of this research lies in addressing the critical question of whether WPC can reliably replace conventional materials in structural components while meeting required performance standards. To enhance stiffness and load-bearing capacity, the integration of WPC into a sandwich panel configuration is proposed, where two thin but strong outer faces are separated by a lightweight core. In this study, the core is composed of glss fiber-reinforced polymer, which is expected to synergistically enhance the mechanical performance of the composite panel. The presented study is particularly valuable as it combines experimental investigation and theoretical modeling to evaluate the structural behavior of WPC-based sandwich panels. Static performance parameters such as failure strength, stiffness, and deflection under applied loads are systematically studied. The findings of this study will provide critical insights into the design and optimization of WPC-based structural members, enabling their safe and effective application in civil and industrial engineering projects. Furthermore, the research contributes to sustainable material development by promoting the use of recycled wood and plastics, thereby supporting environmentally responsible construction practices. Overall, the study addresses a gap in current knowledge regarding the structural applicability of WPC, providing both experimental evidence and theoretical validation that can guide future adoption of this versatile and eco-friendly material in engineering structures.

3. Experimental study

This section presents the experimental program conducted to investigate the flexural behavior of sandwich panels composed of WPC plates and externally bonded GFRP sheets. To evaluate the performance of these panels under floor-type loading conditions, where transverse loads are predominant, a total of eight specimens were prepared. Among them, four panels were tested under concentrated point loading, while the remaining four were subjected to linear loading. The following subsections describe the materials, preparation of specimens, and test procedures.

3.1. Material properties

The WPC plates employed in this research were hollow sections with nominal dimensions of 54 × 54 cm. Their geometry and cross-section are illustrated in Figs. 1 and 2, respectively.

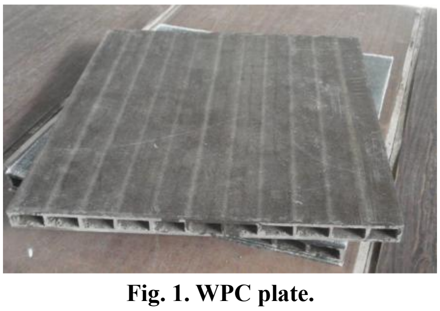

Fig. 1. WPC plate.

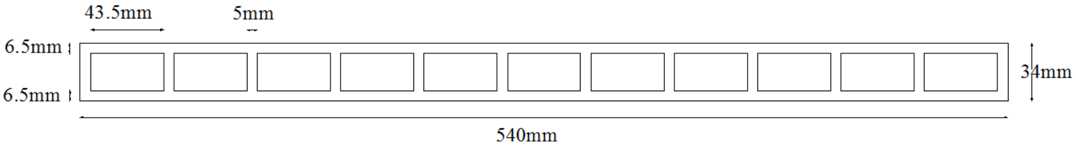

Fig. 2. Cross-section of WPC plate.

The reinforcement consisted of unidirectional glass fiber reinforced polymer (GFRP) sheets, with all fibers aligned in the longitudinal direction (Fig. 3). The mechanical properties of the GFRP sheets, as provided by the manufacturer, are summarized in Table 1.

Fig. 3. Unidirectional GFRP sheets.

Table 1. Mechanical properties of GFRP sheets.

Fiber type	Thickness (mm)	Unit weight (g/mm^2)	Tensile strength (MPa)	Modulus of elasticity (GPa)
GFRP	0.12	420	2300	76

The GFRP sheets were bonded to WPC substrates using a two-component epoxy adhesive consisting of resin and hardener (Fig. 4). The mixing ratio was 2:1 by weight. The epoxy exhibited adequate viscosity for surface application and a pot life of approximately 70 minutes at room temperature. Mechanical properties are summarized in Table 2.

Table 2. Mechanical properties of epoxy adhesive.

Flexural strength (MPa)	Tensile strength (MPa)	Compressive strength (MPa)	Tensile modulus of elasticity (MPa)
78.2	43	130	1560

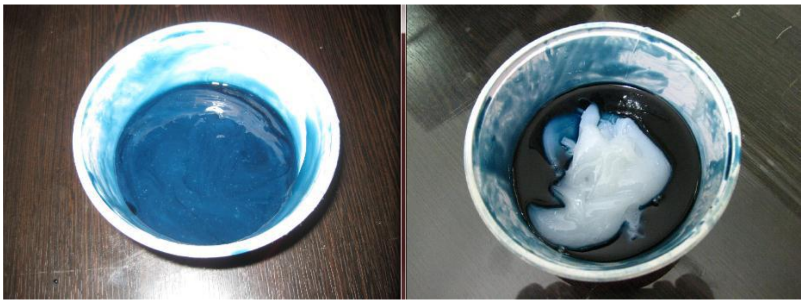

Fig. 4. Epoxy resin and hardener mixture.

3.2. Test specimens and characterization

In order to be able to compare the results obtained through the experiments with analytical and numerical methods, we must have the properties and specifications of the materials. In this study, the adhesive and GFRP sheets were previously tested by the manufacturer in a very precise manner and in accordance with the relevant standards, and this information was available. However, detailed information regarding the behavior of the WPC used was not available, so the strength, initial modulus of elasticity, and the overall behavior of the WPC in compression and tension were determined by uniaxial compressive and tensile tests. These tests are as follows:

3.2.1. Compression test

Compressive strength was determined in accordance with ASTM D695 [21]. Specimens of 25.4 × 12.7 × 12.7 mm were prepared Fig. 5, and a total of seven replicates were tested to minimize experimental error.

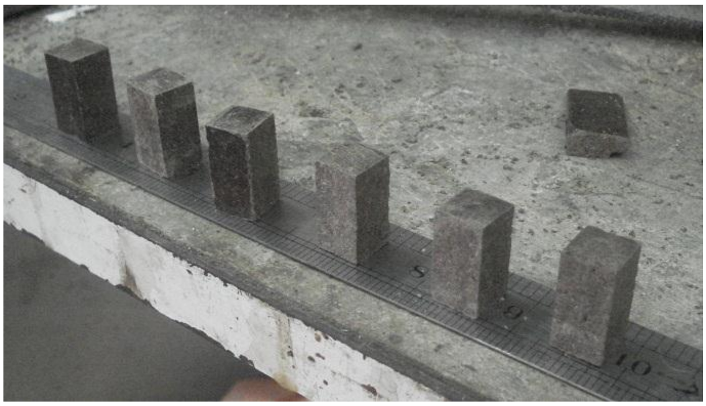

Fig. 5. WPC specimens for compression test.

Loading was applied under displacement control at a rate of 1 mm/min using a universal testing machine (STM-150). The testing setup is shown in Fig. 6.

Fig. 6. Compressive strength test setup.

The results of the compression test are presented in Table 3.

Table 3. Results of the compression test on WPC.

Compressive strength (MPa)	Maximum strain	Initial modulus of elasticity (MPa)
45.798	0.0459	2359

3.2.2. Tensile strength test

According to ASTM D638 [22] standard, tensile specimens were prepared in the specified dimensions as shown in Fig. 7. A milling machine was used to cut and prepare the specimens in the specified dimensions. The specimens for tensile testing are shown in Fig. 8.

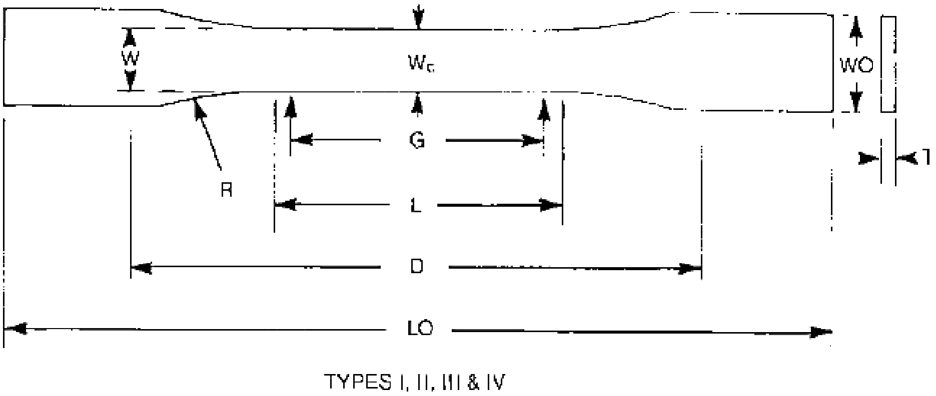

Fig. 7. Geometry of tensile specimens (ASTM D638 [22]).

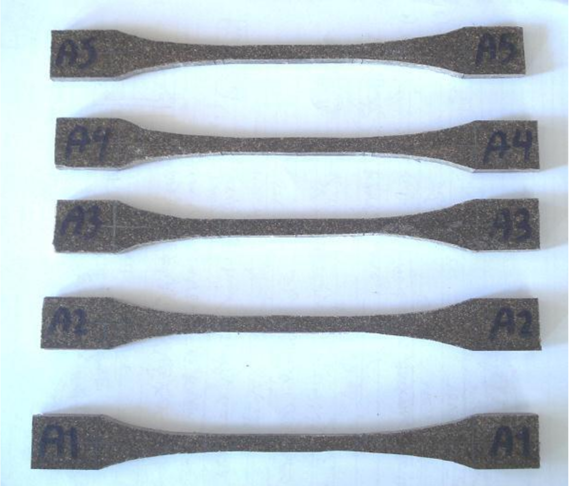

Fig. 8. Prepared tensile specimens.

Loading was applied at 1 mm/min using a universal testing machine (STM-250), as shown in Fig. 9.

Fig. 9. Tensile strength test setup.

The tensile test results are presented in Table 4.

Table 4. Results of the tensile strength test on WPC.

Tensil strength (MPa)	Maximum strain	Initial modulus of elasticity (MPa)
16.578	0.0102	1959.8

3.3. Test specimens (sandwich panels)

Eight sandwich panels were fabricated and categorized into four groups (two specimens per group). The test matrix is summarized in Table 5.

Table 5. Specimen configurations.

Group	GFRP layers (bottom)	GFRP layers (top)
A_0, P_0	0	0
A_1, P_1	1	1
A_2, P_2	1	2
A_3, P_3	1	3

Before gluing the GFRP layers, first the WPC surfaces and GFRP sheets were thoroughly cleaned and wiped so that no dust or dirt remained. Next, the sheets were prepared by cutting the layers to the size of the WPC surfaces, i.e., 54 × 54 cm, and by mixing 160 g of resin and 80 g of hardener, the epoxy adhesive was prepared for gluing. Finally, the GFRP layers were glued by spreading the adhesive evenly on the WPC. The time required to reach maximum adhesive strength was 7 - 10 days, which was taken into account before the test. During preliminary trials, poor bonding was observed due to the glazed finish on the WPC surface, which prevented adequate adhesion.

To resolve this, the surface glaze was removed using a wire brush attached to a grinding machine, resulting in a roughened texture Fig. 10. The final prepared specimens are shown in Fig. 11.

Fig. 10. WPC surface after glaze removal.

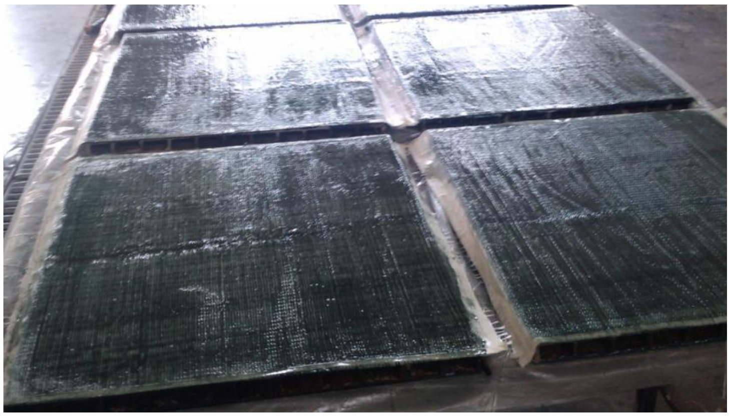

Fig. 11. GFRP bonded to WPC without glazing.

3.4. Test setup and instrumentation

3.4.1 Support configuration

As mentioned in the previous sections, the STM150 universal device was used for the bending test. The support provided for this device was suitable for beams with a maximum width of 15 cm. Since the width of the panels was 54 cm, a suitable support had to be designed to use the device.

3.4.2. Loading attachments

The universal testing machine applies load through a 13 cm linear bearing surface. To simulate two types of loading, concentrated point loading and distributed linear loading across 54 cm, two steel attachments were fabricated. Owing to their high stiffness relative to WPC, steel deformations were considered negligible.

3.5. Loading procedure

The load on the WPC was applied in two ways: point and linear. First, 4 samples (one sample from each group) were subjected to a point load. However, since the results of this loading did not fully satisfy the purpose of this research, the remaining 4 samples were tested as linear loading.

3.5.1. Point loading

As shown in Fig. 12, the span length was set at 54 cm, with hinge supports at both ends.

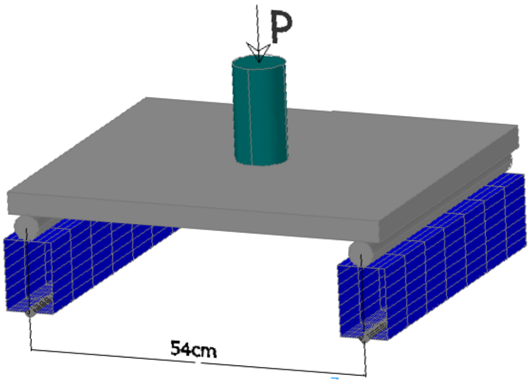

Fig. 12. Point loading schematic view.

The loading was performed under displacement control at a constant rate of 5 mm/min, as recommended by ASTM D790 for quasi-static flexural testing of polymer and composite materials. This rate was selected to ensure stable crack propagation and to minimize dynamic or rate-dependent effects during testing (Fig. 13).

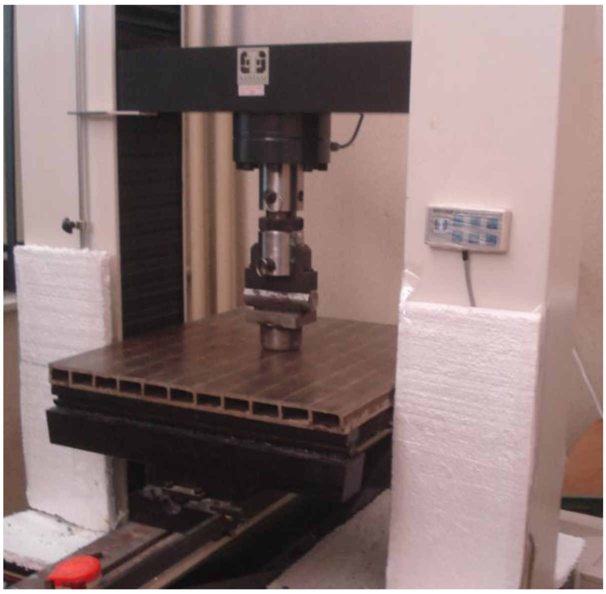

Fig. 13. Experimental setup for point loading.

The loading proceeded to a stage where the WPC-GFRP panel broke, or the force applied to the monitor became close to zero.

3.5.2. Linear Loading

In the second loading configuration, the panels were tested under linear loading conditions Fig. 14, simulating a three-point bending scenario with extended load distribution.

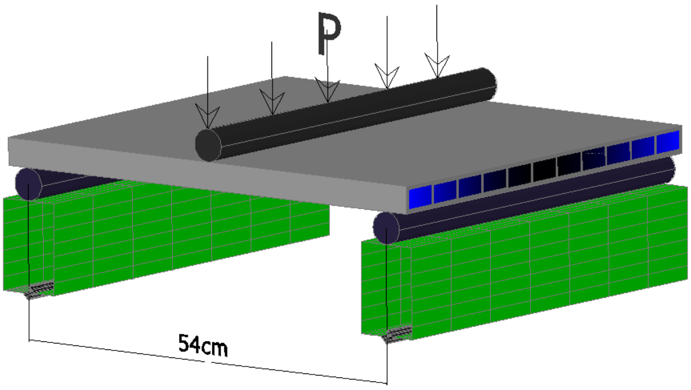

Fig. 14. Linear loading schematic view.

After positioning the steel attachment at midspan, the panels were tested under the same displacement rate of 5 mm/min until failure (Fig. 15).

Fig. 15. Experimental load–deflection curves of WPC–GFRP panels under point loading.

4. Theoretical analysis

The static behavior of the WPC-GFRP sandwich panels was first investigated using theoretical formulations based on composite laminate mechanics, sandwich beam theory, and plate theory.

4.1. Composite laminate mechanics

The GFRP facesheets were modeled as orthotropic elastic laminates, in which the stress–strain relationship follows the generalized Hooke's law for anisotropic media:

$$\sigma_{ii} = C_{ij}.\varepsilon_j \quad , \quad i,j=1......6 \tag{1}$$

Where σ_i represents the stress components, C_{ij} denotes the stiffness matrix coefficients, and ε_j are the strain components. For small deformations, the strain–displacement relations are given by:

$$\begin{gathered}\varepsilon_x = \frac{\delta_u}{\delta_x}, \qquad \varepsilon_y = \frac{\delta_v}{\delta_y}, \qquad \varepsilon_z = \frac{\delta_w}{\delta_z} \\ \varepsilon_{xz} = \frac{1}{2}\left(\frac{\delta_u}{\delta_z} + \frac{\delta_w}{\delta_x}\right), \qquad \varepsilon_{yz} = \frac{1}{2}\left(\frac{\delta_v}{\delta_z} + \frac{\delta_w}{\delta_y}\right), \qquad \varepsilon_{xz} = \frac{1}{2}\left(\frac{\delta_u}{\delta_y} + \frac{\delta_v}{\delta_x}\right)\end{gathered} \tag{2}$$

The strain energy density increment is expressed as:

$$d\mathrm{w} = \sigma_i.d\varepsilon_i \tag{3}$$

In these relations, *u*, *v*, and *w* denote the displacements along the *x*, *y*, and *z* directions, respectively, and the partial derivatives represent the spatial deformation components under small strain assumptions. which yields the total strain energy as:

$$w = \frac{1}{2} C_{ij}.\varepsilon_i.\varepsilon_j \tag{4}$$

By taking the derivative of the strain energy with respect to ε_i and ε_j, the following relations are obtained:

$$\frac{\partial W}{\partial \varepsilon_i \partial \varepsilon_j} = C_{ij} \tag{5}$$

$$\frac{\partial W}{\partial \varepsilon_j \partial \varepsilon_i} = C_{ij} \tag{6}$$

Comparing Eqs. 5 and 6, it is concluded that the stiffness matrix is symmetric, that is:

$$C_{ij} = C_{ji} \tag{7}$$

For this reason, the number of independent coefficients in the stiffness matrix is reduced from 36 to 21. A similar symmetry also holds for the softness matrix (*S*):

$$S_{ij} = S_{ji} \tag{8}$$

Therefore, the general relationship between stress and strain will be in the following matrix form:

$$\begin{Bmatrix}\sigma_1\\ \sigma_2\\ \sigma_3\\ \sigma_{23}\\ \sigma_{31}\\ \sigma_{12}\end{Bmatrix} = \begin{bmatrix} C_{11} & C_{12} & C_{13} & C_{14} & C_{15} & C_{16}\\ C_{21} & C_{22} & C_{23} & C_{24} & C_{25} & C_{26}\\ C_{31} & C_{32} & C_{33} & C_{34} & C_{35} & C_{36}\\ C_{41} & C_{42} & C_{43} & C_{44} & C_{45} & C_{46}\\ C_{51} & C_{52} & C_{53} & C_{54} & C_{55} & C_{56}\\ C_{61} & C_{62} & C_{63} & C_{64} & C_{56} & C_{66}\end{bmatrix} * \begin{Bmatrix}\varepsilon_1\\ \varepsilon_2\\ \varepsilon_3\\ \gamma_{23}\\ \gamma_{31}\\ \gamma_{12}\end{Bmatrix} \tag{9}$$

The stiffness matrix becomes simpler depending on the number of symmetry planes in the material:

$$\begin{Bmatrix}\sigma_1\\ \sigma_2\\ \sigma_3\\ \tau_{23}\\ \tau_{31}\\ \tau_{12}\end{Bmatrix} = \begin{bmatrix} C_{11} & C_{12} & C_{13} & 0 & 0 & C_{16}\\ & C_{22} & C_{23} & 0 & 0 & C_{26}\\ & & C_{33} & C_{34} & 0 & C_{36}\\ & & & C_{44} & C_{45} & C_{46}\\ & sym & & & C_{55} & C_{56}\\ & & & & & C_{66}\end{bmatrix} * \begin{Bmatrix}\varepsilon_1\\ \varepsilon_2\\ \varepsilon_3\\ \gamma_{23}\\ \gamma_{31}\\ \gamma_{12}\end{Bmatrix} \tag{10}$$

Two or three perpendicular planes (orthotropic):

$$\begin{Bmatrix}\sigma_1\\ \sigma_2\\ \sigma_3\\ \tau_{23}\\ \tau_{31}\\ \tau_{12}\end{Bmatrix} = \begin{bmatrix} C_{11} & C_{12} & C_{13} & 0 & 0 & 0\\ & C_{22} & C_{23} & 0 & 0 & 0\\ & & C_{33} & 0 & 0 & 0\\ & & & C_{44} & 0 & 0\\ & sym & & & C_{55} & 0\\ & & & & & C_{66}\end{bmatrix} * \begin{Bmatrix}\varepsilon_1\\ \varepsilon_2\\ \varepsilon_3\\ \gamma_{23}\\ \gamma_{31}\\ \gamma_{12}\end{Bmatrix} \tag{11}$$

Lateral isotropic:

$$\begin{Bmatrix}\sigma_1\\ \sigma_2\\ \sigma_3\\ \tau_{23}\\ \tau_{31}\\ \tau_{12}\end{Bmatrix}=\begin{bmatrix}C_{11} & C_{12} & C_{13} & 0 & 0 & 0\\ & C_{22} & C_{23} & 0 & 0 & 0\\ & & C_{33} & 0 & 0 & 0\\ & & & C_{44} & 0 & 0\\ & sym & & & C_{55} & 0\\ & & & & & \dfrac{(C_{11}-C_{12})}{2}\end{bmatrix}*\begin{Bmatrix}\varepsilon_1\\ \varepsilon_2\\ \varepsilon_3\\ \gamma_{23}\\ \gamma_{31}\\ \gamma_{12}\end{Bmatrix} \tag{12}$$

Perfect isotropic:

$$\begin{Bmatrix}\sigma_1\\ \sigma_2\\ \sigma_3\\ \tau_{23}\\ \tau_{31}\\ \tau_{12}\end{Bmatrix}=\begin{bmatrix}C_{11} & C_{12} & C_{13} & 0 & 0 & 0\\ & C_{22} & C_{23} & 0 & 0 & 0\\ & & C_{33} & 0 & 0 & 0\\ & & & \dfrac{(C_{11}-C_{12})}{2} & 0 & 0\\ & sym & & & \dfrac{(C_{11}-C_{12})}{2} & 0\\ & & & & & \dfrac{(C_{11}-C_{12})}{2}\end{bmatrix}*\begin{Bmatrix}\varepsilon_1\\ \varepsilon_2\\ \varepsilon_3\\ \gamma_{23}\\ \gamma_{31}\\ \gamma_{12}\end{Bmatrix} \tag{13}$$

For the orthotropic case, the coefficients $C_{ij}=C_{ji}$ are calculated based on Young's moduli, Poisson's ratios, and shear moduli. Eqs. 14 to 18 show these dependencies.

$$C_{11}=\frac{1-v_{23}v_{32}}{E_2E_3\Delta}\qquad C_{22}=\frac{1-v_{13}v_{31}}{E_1E_3\Delta}\qquad C_{33}=\frac{1-v_{12}v_{21}}{E_1E_2\Delta} \tag{14}$$

$$C_{12}=\frac{v_{21}+v_{31}v_{23}}{E_2E_3\Delta}=\frac{v_{21}+v_{32}v_{13}}{E_1E_3\Delta} \tag{15}$$

$$C_{23}=\frac{v_{32}+v_{12}v_{31}}{E_1E_3\Delta}=\frac{v_{23}+v_{21}v_{13}}{E_1E_2\Delta} \tag{16}$$

$$C_{13}=\frac{v_{31}+v_{21}v_{32}}{E_2E_3\Delta}=\frac{v_{13}+v_{12}v_{23}}{E_1E_2\Delta} \tag{17}$$

$$C_{44}=G_{23},\quad C_{55}=G_{31},\quad C_{66}=C_{13}$$

$$\Delta=\frac{1-v_{12}v_{23}-v_{23}v_{32}-v_{31}v_{13}-2(v_{12}v_{23}v_{13})}{E_1E_2E_3} \tag{18}$$

The important point is that these relations are valid for a layer whose fiber axis is aligned with the axes. However, in practice there is usually an angle between the fibers and the axes. For this purpose, the transfer matrix Eq. 19 must be used to calculate the stiffness values in the new coordinate system.

$$\begin{Bmatrix}\sigma_x\\ \sigma_y\\ \sigma_{xy}\end{Bmatrix}=\begin{bmatrix}cos_a^2 & sin_a^2 & -2sinacosa\\ sin_a^2 & cos_a^2 & 2sinacosa\\ sinacosa & -sinacosa & cos_a^2-sin_a^2\end{bmatrix}\begin{Bmatrix}\sigma_x\\ \sigma_y\\ \sigma_{xy}\end{Bmatrix} \tag{19}$$

For the plane stress case, Eq. 20 express the relationship between the stiffness matrix Q, the transfer matrix T, and the transferred stiffness matrix $\bar{Q}$. When the lamina axes are rotated with respect to the global coordinate system, the transformed reduced stiffness matrix is:

$$\begin{Bmatrix}\sigma_x\\ \sigma_y\\ \sigma_{xy}\end{Bmatrix}_k=[\bar{Q}]_k\begin{Bmatrix}\varepsilon_x\\ \varepsilon_y\\ \varepsilon_{xy}\end{Bmatrix}_k\qquad \text{and}\qquad [\bar{Q}]_k=[T]_k^{-1}[Q]_k[T]_k^{-1} \tag{20}$$

4.2. Levy solution for rectangular sheet

To investigate the elastic behavior of rectangular plates under loading, Levy's method is used. This method is based on the equations governing the bending of plates in the classical theory of elasticity. The governing differential equation for the transverse displacement *w(x,y)* is expressed as follows:

$$\frac{\partial^4 w}{\partial x^4}+2\frac{\partial^4 w}{\partial x^2\partial y^2}+\frac{\partial^4 w}{\partial y^4}=\frac{p(x,y)}{D} \tag{21}$$

Where D is the flexural rigidity of the plate ($D=Eh^3/12(1-\nu^2)$), $w(x,y)$ is the transverse displacement, $q(x,y)$ is the distributed transverse load, E is the elastic modulus, h is the thickness of the plate, and v is Poisson's ratio.

The Levy method can be used for a rectangular sheet where two opposite supports (for example, supports $x=0$ and $x=a$) are the same and the other two supports ($y=\pm b/2$) are arbitrary. The general solution in this method includes the general solution w_h and the particular solution w_p, which is equal to:

$$w_h = \sum\nolimits_{m=1}^{\infty} \left(A_m \, sinh \frac{m\pi x}{a} + B_m cosh \frac{m\pi x}{a} + C_m y cosh \frac{m\pi x}{a} + D_m y cosh \frac{m\pi x}{a} \right) \tag{22}$$

In order to satisfy the boundary conditions of the sheet at the edges x = 0 and $x = a$, the particular solution can be expressed as the Fourier series of Eq. 23.

$$w_p = \sum\nolimits_{m=1}^{\infty} k_m(y) \frac{sin \; m\pi x}{a} \tag{23}$$

$$p(x,y) = \sum\nolimits_{m=1}^{\infty} p_m(y) \frac{sin \; m\pi x}{a} \tag{24}$$

$$p_m(y) = \frac{2}{a} \int_{\frac{a}{2}+\xi}^{\frac{a}{2}+\xi} p(x,y) \frac{sin \; m\pi x}{a} dx$$

$$p(x,y) = \frac{p_0}{\xi} \tag{25}$$

$$\lim_{\xi \to 0} p_m(y) = \frac{2p_0}{a}$$

By substituting Eqs. 23 and 24 into Eq. 21, given that the obtained equation should yield results for all values of x between 0 and a.

$$\frac{d^4 k_m}{dy^4} - 2\left(\frac{m\pi}{a}\right)^2 \frac{d^2 k_m}{dy^2} + \left(\frac{m\pi}{a}\right)^4 k_m = \frac{p_m}{D} \tag{26}$$

For the case $P(x,y) = P_0$, it follows from Eq. 25;

$$p_m = \frac{2p_0}{a} \qquad (m = 1, 3, \dots) \tag{27}$$

$$w_p = \frac{2p_0 a^3}{\pi^4 D} \sum\nolimits_{m=1}^{\infty} \frac{1}{m^4} \frac{sin \; m\pi x}{a} \tag{28}$$

By selecting axes, the deflection of the sheet must be symmetrical about the x-axis. In other words, the deflections for +y and -y must be equal. Consequently, the total deflection of the sheet is equal to:

$$W = \sum\nolimits_{m=1,3,\dots}^{\infty} \left(B_m cosh \frac{m\pi x}{a} + C_m y cosh \frac{m\pi x}{a} + \frac{2p_0 a^3}{m^4 \pi^4 D} \right) \frac{sin \; m\pi x}{a} \tag{29}$$

Putting these two boundary conditions into Eq. 29, we have:

$$B_m = -\left(\frac{2a^3 Pv(bm\pi)(-1+v) cosh \left[\frac{bm\pi}{2a}\right] + 2a(1+v) \, sinh \left[\frac{bm\pi}{2a}\right]}{Dm^4 \pi^4 \big(bm\pi(-1+v)\big) + a(3+v) \, sinh \left[\frac{bm\pi}{2a}\right]} \right) \tag{30}$$

$$C_m = -\left(\frac{4a^3 Pv(bm\pi) \, sinh \left[\frac{bm\pi}{2a}\right]}{Dm^3 \pi^3 (-1+v)\big(bm\pi(-1+v)\big) + a(3+v) \, sinh \left[\frac{bm\pi}{2a}\right]} \right) \tag{31}$$

So we have:

$$\begin{aligned} W_{max} = {} & \sum\nolimits_{m=1,3,\dots}^{\infty} \left(\frac{1}{Dm^4 \pi^4 \big(bm\pi(-1+v)\big) + a(3+v) \, sinh \left[\frac{bm\pi}{2a}\right]} \right) 2a^3 p \, sin \left[\frac{m\pi}{2}\right] \\ & \Bigg(-bm\pi(-1+v)v \cosh \left[\frac{bm\pi}{2a}\right] - 2av\,(1+v) \sinh \left[\frac{bm\pi}{2a}\right] \\ & \quad + (-1+v) \left(bm\pi(-1+v) + a(3+v) \sinh \left[\frac{bm\pi}{2a}\right] \right) \Bigg) \end{aligned} \tag{32}$$

4.3. Bending theory of WPC-GFRP sandwich panels

When a beam is subjected to concentrated forces, self-weight, or applied couples, bending moments are generated, which lead to deformation. Under the action of external loads, the upper fibers of the beam shorten and are thus in compression, while the lower fibers elongate and are subjected to tension. The line dividing the compression and tension regions, along which no strain occurs, is defined as the neutral axis (NA). Experimental uniaxial tests on WPC revealed that its mechanical response in both compression and tension is nonlinear, indicating deviation from Hooke's law. Furthermore, the material exhibits asymmetric behavior in compression and tension. To capture this nonlinear response, curve fitting was performed on the stress–strain diagrams, leading to the constitutive relation:

$$\sigma = A\varepsilon^2 + B\varepsilon \tag{33}$$

Where σ_c and σ_t are the compressive and tensile stresses in the WPC core, respectively; ε_c and ε_t are the corresponding strains; and a, b, c, and d are regression constants derived from the experimental stress–strain data.

For the GFRP reinforcement, a linear elastic relationship was assumed up to failure:

$$\sigma_{frp} = E_{frp}\varepsilon_{frp} \tag{34}$$

Where σ_f and ε_f are the stress and strain in the GFRP reinforcement, E_f is the elastic modulus of the GFRP layer, and the response is assumed linear up to failure.

The tested WPC-GFRP cross-section can be idealized as an assembly of I-shaped elements. Due to symmetry in geometry, loading, and support conditions, shear stresses between adjacent elements can be neglected, allowing the analysis of a single equivalent I-beam subjected to the same distributed load. Considering the linear distribution of strain across the section depth, the following strain relations for the face and core fibers can be written:

$$\varepsilon_{fm} = \frac{\varepsilon_{top}\left(H - h + t_{frp}\right)}{h} \tag{35}$$

$$\varepsilon_{wm} = \frac{\varepsilon_{top}(H - h)}{h} \tag{36}$$

By substituting the constitutive models (Eqs. 33 and 34) into the equilibrium condition, the axial force balance (Eq. 37), bending moment capacity (Eq. 38), and maximum shear force (Eq. 39) are obtained. Furthermore, considering the linear strain distribution:

$$\begin{aligned}\int_0^h b_f[A\varepsilon^2 + B\varepsilon]dy - \int_0^{h-t_f}\left(b_f - t_w\right)[A\varepsilon^2 + B\varepsilon]dy + A_{frp}E_{frp}\varepsilon_{frp} - \\ \int_0^{H-h} b_f'\left[A'^{\varepsilon^2} + B'\varepsilon\right]dy + \int_0^{H-h-t_f'}\left(b'_f - t_w\right)\left[A'^{\varepsilon^2} + B'\varepsilon\right]dy + A'_{frp}E_{frp}\varepsilon'_{frp} = 0\end{aligned} \tag{37}$$

$$\begin{aligned}M = \int_0^h b_f[A\varepsilon^2 + B\varepsilon]ydy - \int_0^{h-t_f}\left(b_f - t_w\right)[A\varepsilon^2 + B\varepsilon]ydy + A_{frp}E_{frp}\varepsilon_{frp}\left(h + \frac{t_{frp}}{2}\right) \\ - \int_0^{H-h} yb_f'\left[A'^{\varepsilon^2} + B'\varepsilon\right]dy \\ + \int_0^{H-h-t_f'}\left(b'_f - t_w\right)\left[A'^{\varepsilon^2} + B'\varepsilon\right]ydy + A'_{frp}E_{frp}\varepsilon'_{frp}\left(H - h + \frac{t'_{frp}}{2}\right)\end{aligned} \tag{38}$$

$$V_{max} = \int_0^h b_f[A\varepsilon^2 + B\varepsilon]dy - \int_0^{h-t_f}\left(b_f - t_w\right)[A\varepsilon^2 + B\varepsilon]dy + A_{frp}E_{frp}\varepsilon_{frp} \tag{39}$$

$$\varepsilon = \frac{\varepsilon_{top}y}{h} \tag{40}$$

In the above relations, M the bending moment, V the shear force, σ and ε the stress and strain distributions across the section depth h and y the distance from the neutral axis.

By substituting into the governing relations yields the simplified expressions for bending moment and shear capacity:

$$\begin{aligned}M = \frac{1}{6h^2}\varepsilon_{top}\big(3Bb_fh^3 + 2Ab_f\varepsilon_{top}h^3 - b'_f(h - H)^2\big(3B'h + 2A\varepsilon_{top}(h - H) + \\ 3A_{frp}E_{frp}h\left(2h + t_{frp}\right) + 3A'_{frp}E_{frp}h\left(2h + 2H - t'_{frp}\right) - \left(3Bh + 2A\varepsilon_{top}\left(h - t_f\right)\right. \\ \left(h - t_f\right)^2\left(b_f - t_w\right) + \left(h - H + {t'_f}^2\right)\left(3B'h - 2A'\varepsilon_{top}\left(h - H - t'_f\right)\left(b'_f - t_w\right) = 0\end{aligned} \tag{41}$$

$$\begin{aligned}V_{max} = \tfrac{1}{6h^2}\varepsilon_{top}\left(3Bb_fh^3 + 2Ab_f\varepsilon_{top}h^3 + 3A_{frp}E_{frp}h\left(2h + t_{frp}\right)\right. - \left(3B\,h + 2A\varepsilon_{top}\right(h - \\ t_f\left)\right)\left(h - t_f\right)^2\left(b_f - t_w\right)\end{aligned} \tag{42}$$

Where M and V represent the ultimate bending moment and shear capacity, respectively, and $\tau_{\max}$ denotes the maximum shear stress developed within the core.

Two primary failure criteria are considered in the bending analysis:

- Flexural failure: occurs when the compressive or tensile strain at the extreme fibers reaches the ultimate strain capacity.
- Shear failure: occurs when the core shear stress exceeds its maximum allowable shear strength.

The bending response of the WPC-GFRP sandwich section is therefore governed by the interaction between the nonlinear behavior of the WPC core and the linear elastic contribution of the GFRP layers, with failure predicted by the most critical of the two mechanisms.

5. Numerical method

The Finite element method (FEM) is a powerful numerical tool for solving engineering problems and encompasses a wide range of analyses. This method is applied not only in structural analysis but also in diverse physical problems, including heat transfer, seepage, fluid flow, and electric or magnetic potential. Generally, analyzing an engineering problem requires developing a mathematical model representing the physical conditions. The mathematical model of a geometric problem is referred to as the governing equations of the problem. These governing equations are primarily differential equations accompanied by initial and boundary conditions. Differential equations are derived by applying fundamental laws, such as the conservation of mass, force, and energy, to an infinitesimal element of the system.

In FEM, the differential equations for each element are solved using interpolation functions, and the element-level governing equations are obtained. By assembling the equations of all elements, the global governing equations of the entire model are formed. Ultimately, these differential equations are replaced with a system of linear or nonlinear algebraic equations for numerical solution. For complex geometries, FEM modeling can be time-consuming and costly. Using FEM software significantly reduces this difficulty. One widely used FEM software is ABAQUS, which has gained prominence in research and industry worldwide due to its flexibility and capability to solve diverse engineering problems. In this study, ABAQUS was employed to implement the numerical analysis.

5.1. Development of a numerical model

To create an analytical model, several steps are followed. First, the general configuration of the structure must be defined, followed by the material behavior of the structural components. Key considerations include yield criteria, hardening, and the transition to plastic behavior. Next, structural components are defined according to geometry and material. The choice of element type influences system behavior and must be based on understanding element characteristics, response under applied loads, location in the model, relative dimensions, and experience from similar analyses.

After defining all elements, they are assembled into a complete structure, meshed, and boundary conditions are applied. Loading is then introduced to prepare the model for analysis.

In this study, WPC-GFRP sandwich panels with dimensions 54×54 cm were tested experimentally. The geometric properties of these samples were first defined in ABAQUS using the Part module. Solid extrusion was used for WPC and steel sections, while shell elements were applied for GFRP sheets. Detailed geometries are illustrated in Fig. 16.

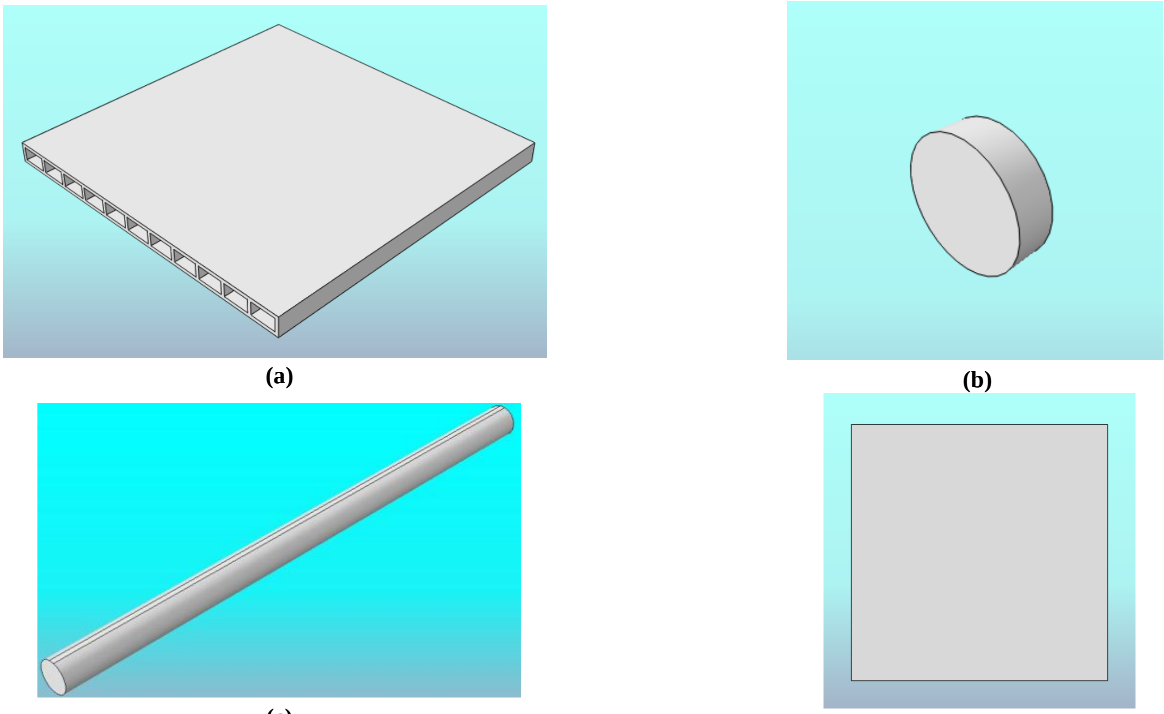
(a) **(b)**

(c) **(d)**

Fig. 16. Developed segments: (a) WPC drawing, (b) Drawing of steel part (for point loading), (c) Drawing of a steel part (for linear loading), and (d) Drawing of GFRP sheets.

5.2. Material modeling

For point-loading simulations, a material with arelatively high elastic modulus is required. Steel sections used in the study exhibit such stiffness and are modeled as isotropic elastic with E = 210 GPa and Poisson's ratio v = 0.3. Isotropic materials have identical elastic properties in all directions, and their stress-strain relationship is given by:

$$\varepsilon_{11} = \frac{\sigma_{11}}{E} - \frac{v}{E}(\sigma_{22} + \sigma_{33}) \tag{43}$$

$$\varepsilon_{22} = \frac{\sigma_{22}}{E} - \frac{v}{E}(\sigma_{11} + \sigma_{33})$$
$$\varepsilon_{11} = \frac{\sigma_{33}}{E} - \frac{v}{E}(\sigma_{11} + \sigma_{22})$$
$$\gamma_{11} = \frac{\tau_{12}}{G}, \gamma_{13} = \frac{\tau_{13}}{G}, \gamma_{23} = \frac{\tau_{23}}{G}$$

The shear modulus is computed as:

$$G = \frac{E}{2(1+v)} \tag{44}$$

The elastic coefficient matrix for isotropic materials is given in Eq. 45.

$$[D] = \begin{bmatrix} \frac{1}{E} & \frac{-v}{E} & \frac{-v}{E} & 0 & 0 & 0 \\ \frac{-v}{E} & \frac{1}{E} & \frac{-v}{E} & 0 & 0 & 0 \\ \frac{-v}{E} & \frac{-v}{E} & \frac{1}{E} & 0 & 0 & 0 \\ 0 & 0 & 0 & \frac{1}{G} & 0 & 0 \\ 0 & 0 & \frac{-v}{E} & 0 & \frac{1}{G} & 0 \\ 0 & 0 & \frac{1}{E} & 0 & 0 & \frac{1}{G} \end{bmatrix} \tag{45}$$

Where σ and ε are the stress and strain tensors, E is the elastic modulus, v is Poisson's ratio, and G is the shear modulus of elasticity. The matrix C represents the constitutive stiffness matrix for isotropic elastic materials.

Experimental results indicated that WPC exhibits nonlinear and distinct tensile and compressive behavior. In ABAQUS, such behavior was modeled using the Cast Iron material option, which accommodates nonlinear plastic behavior. Although the material behaves elastically throughout the experiment, this approach accurately represents its mechanical response. Although wood–plastic composites (WPCs) generally exhibit viscoelastic characteristics under long-term or cyclic loading, such effects are insignificant in the present study because all tests and numerical simulations were conducted under monotonic static loading until failure. Therefore, the primary focus of the modeling was to reproduce the nonlinear stress–strain response and tension–compression asymmetry rather than time-dependent creep or relaxation behavior. The Cast Iron Plasticity model in ABAQUS was selected for this purpose because it provides the capability to define distinct tensile and compressive stress–strain relationships and allows for stiffness degradation after yielding, consistent with the observed experimental response. This approach has also been successfully applied in recent studies on quasi-brittle and polymer-based composites under monotonic loading [4, 16]. The WPC material exhibits distinct tension and compression characteristics, as confirmed by the experimental results presented in Section 3.2. To accurately represent this nonlinear and asymmetric behavior, the Cast Iron Plasticity model in ABAQUS was adopted. Although this constitutive option is typically used for materials that undergo nonlinear plastic deformation, it is also suitable for modeling materials with different tensile and compressive responses under monotonic loading. In this study, the applied load was gradually increased until failure, without any unloading or reloading cycles. Therefore, even if the material response remains mostly elastic during loading, the use of the Cast Iron Plasticity model does not contradict the actual structural behavior and enables a more realistic definition of the nonlinear region.

In implementing this model, the elastic behavior was first defined based on the initial linear portion of the stress–strain curve, where the elastic modulus (E) was set equal to the initial slope. The nonlinear plastic region was then introduced by converting the experimental stress–strain data into true stress–plastic strain form. For each data point, the corresponding plastic strain was obtained by subtracting the elastic strain (σ/E) from the total strain (ε_t). The resulting point-by-point data were entered into ABAQUS separately for compression and tension to define the complete material response (as shown in Fig.17). This modeling approach enables the finite element simulation to capture the gradual stiffness degradation and ultimate failure behavior of the WPC material with high fidelity.

Table 6. Input parameters of the WPC material model implemented in ABAQUS.

Parameter	Symbol/Unit	Description	Source/Note
Elastic modulus (compression)	$E_c = 2359$ MPa	Initial elastic stiffness in compression, obtained from the slope of the stress–strain curve in the elastic region.	Experimental uniaxial compression test (Section 3.2).
Elastic modulus (tension)	$E_t = 1959.8$ MPa	Initial elastic stiffness in tension, obtained from the slope of the stress–strain curve in the elastic region.	Experimental uniaxial tension test (Section 3.2).
Poisson's ratio	$v = 0.35$	Ratio of lateral to longitudinal strain.	Typical value for wood–plastic composites.
Compressive strength	$f_c = 45.8$ MPa	Ultimate compressive stress of WPC.	Experimental data (Table 3).

Tensile strength	f_t = 16.6 MPa	Ultimate tensile stress of WPC.	Experimental data (Table 4).
Maximum compressive strain	$\varepsilon_{c,u}$ = 0.049	Strain corresponding to compressive failure.	Derived from the experimental stress–strain curve.
Maximum tensile strain	$\varepsilon_{t,u}$ = 0.0102	Strain corresponding to tensile failure.	Derived from the experimental stress–strain curve.
Plastic strain definition	-	Plastic strain calculated as $\varepsilon_p=\varepsilon-\sigma/E$, introduced point-by-point for both tension and compression.	Converted from true stress–strain data.
Failure model	-	*Cast Iron Plasticity* (separate input curves for tension and compression).	ABAQUS 2023 material model.
Damage behavior	-	Gradual stiffness degradation beyond ultimate stress; no unloading–reloading considered.	Calibrated with experimental load–deflection data.
Element type	-	C3D8R – 8-node brick element with reduced integration.	Used for WPC core.

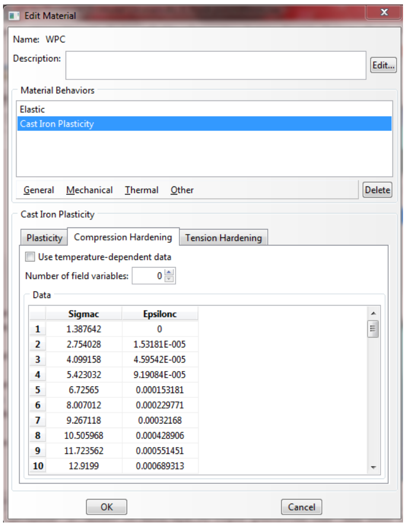

Name: WPC

Description:

Material Behaviors

Elastic

Cast Iron Plasticity

Cast Iron Plasticity

☐ Use temperature-dependent data

Number of field variables: 0

Data

	Sigmac	Epsilonc
1	1.387642	0
2	2.754028	1.53181E-005
3	4.099158	4.59542E-005
4	5.423032	9.19084E-005
5	6.72565	0.000153181
6	8.007012	0.000229771
7	9.267118	0.00032168
8	10.505968	0.000428906
9	11.723562	0.000551451
10	12.9199	0.000689313

Fig. 17. Definition of WPC materials.

Initially, the elastic portion of the material is defined with a modulus equal to the initial slope of the stress-strain curve, followed by input of plastic stress-strain points.

This arrangement produces an orthotropic material, whose mechanical properties differ along the three Cartesian axes Fig. 18.

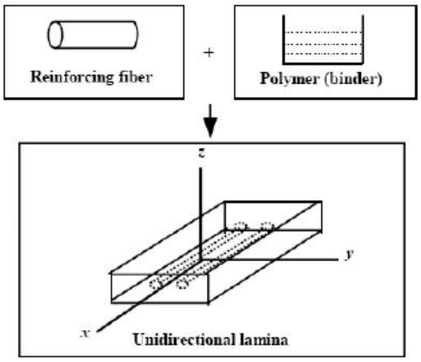

Fig. 18. Schematic diagram of FRP composites.

5.3. Assembly and interaction

After assigning material properties and GFRP layer thickness, the components are assembled using the Assembly module, placing GFRP layers above and below the WPC panel. For point loading, a steel piece is placed at the center of the top layer. Interaction between WPC and GFRP layers is defined using Tie constraints.

Boundary conditions replicate the experimental setup, with roller supports applied at two panel edges to restrict vertical displacement. Displacement-controlled loading is applied to match laboratory conditions Fig. 19.

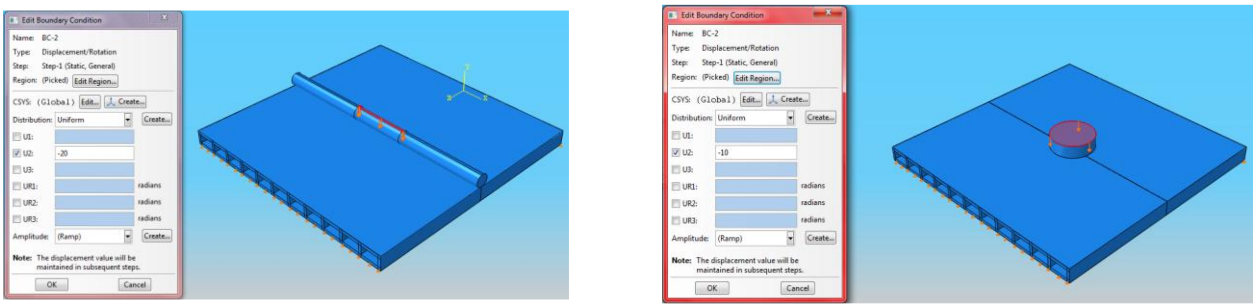

Name: BC-2
Type: Displacement/Rotation
Step: Step-1 (Static, General)
Region: (Picked)
CSYS: (Global)
Distribution: Uniform
☐ U1:
☑ U2: -20
☐ U3:
☐ UR1: radians
☐ UR2: radians
☐ UR3: radians
Amplitude: (Ramp)
Note: The displacement value will be maintained in subsequent steps.

(a)

Name: BC-2
Type: Displacement/Rotation
Step: Step-1 (Static, General)
Region: (Picked)
CSYS: (Global)
Distribution: Uniform
☐ U1:
☑ U2: -10
☐ U3:
☐ UR1: radians
☐ UR2: radians
☐ UR3: radians
Amplitude: (Ramp)
Note: The displacement value will be maintained in subsequent steps.

(b)

Fig. 19. Schematic view of (a) linear loading, and (b) point loading.

Mesh discretization was performed for all model components. GFRP sheets were modeled using S4R shell elements, a 4-node quadrilateral element with reduced integration suitable for bending Fig. 20.

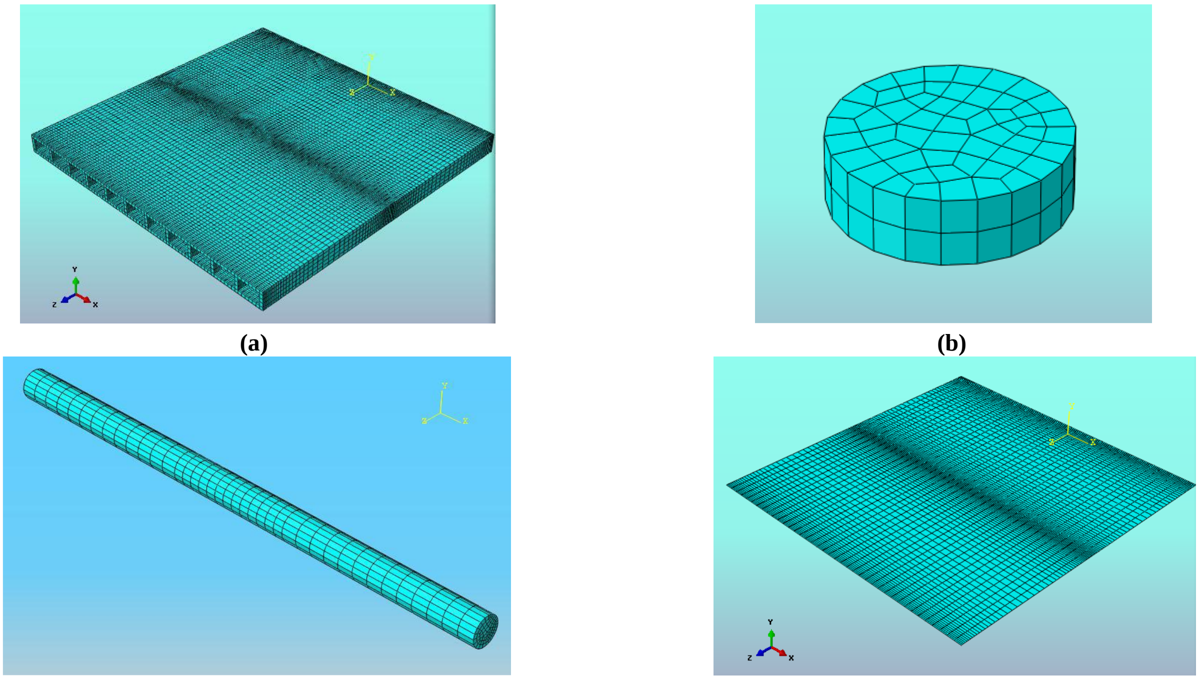

(a) **(b)**

(c) **(d)**

Fig. 20. Meshing: (a) WPC mesh, (b) steel part meshing (point load), (c) meshing of steel part (linear load), and (d) GFRP sheet mesh.

6. Experimental results and discussion

6.1. Failure mode

In the previous sections, the experimental procedures as well as the theoretical and numerical aspects of the WPC-GFRP panels were discussed. Before analyzing the diagrams and the results obtained from the loading tests of the specimens, it is necessary to first describe the possible failure modes of these types of panels. A sandwich structure, in addition to exhibiting high stiffness, must also possess high strength. Four distinct failure modes can occur in sandwich structures subjected to flexural loads. The failure occurs in the mode that develops under the lowest applied load.

- Tensile face sheet failure (or tensile face sheet yielding)

This mode of failure occurs when the normal tensile stresses induced by the applied load exceed the yield strength of the face sheets. Fig. 21a illustrates this type of failure.

- Face sheet wrinkling (or buckling over the core)

This failure mode occurs when the compressive stresses become sufficiently large, causing the face sheets to lose stability. Fig. 21b illustrates this type of failure.

- Core shear failure (or core failure)

This type of failure mode typically occurs when the shear stress within the core exceeds its shear strength. The shear strength of the core depends on factors such as the core material density, the geometry of the core cells, and the thermal conductivity of the core. Fig. 21c illustrates this failure mode.

- Debonding between face sheet and core (or bond failure)

This failure mode occurs when stresses in the adhesive interface become excessive, leading to separation between the face sheet and the core. Fig. 21d illustrates this failure.

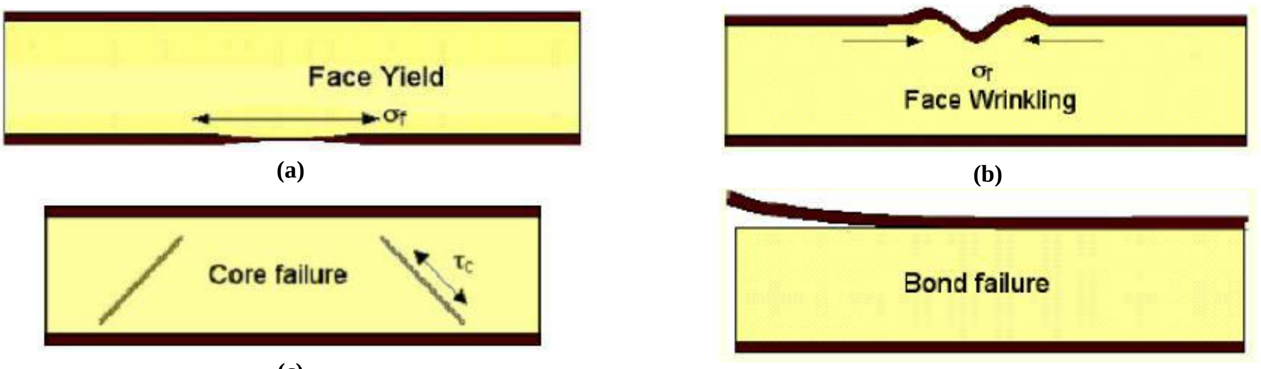

(a) (b) (c) (d)

Fig. 21. Distinct failure modes can occur in sandwich structures subjected to flexural loads: (a) tensile face sheet failure, (b) face sheet wrinkling, (c) core shear failure, and (d) debonding between face sheet and core.

As shown in Fig. 22a, specimen A0 failed at the midspan. This type of failure corresponds to the first mode, occurring in a flexural manner, such that the bottom region under tension yielded first, followed by complete fracture of the entire section. In specimen A1, with a single reinforcement layer on both the top and bottom surfaces, shear cracks developed in the WPC section due to its relatively lower shear capacity compared to flexural capacity. Upon reaching the ultimate load and the subsequent failure of the WPC section, a significant amount of shear was transferred between the GFRP layers and the WPC, leading to debonding at the WPC-GFRP interface. As shown in Fig. 22b, this type of failure corresponds to Mode 4, commonly referred to as debonding. In specimens A2 and A3, the increased stiffness of the section resulted in higher shear forces being transferred to the panel core. Due to the weakness of the joints connecting the WPC plates, the shear force could not be fully transmitted at the ultimate load. Consequently, before debonding occurred between the face sheets and the core, shear failure developed at the joint between the web and flange of the WPC. As illustrated in Fig. 22c, this type of failure corresponds to Mode 3, as described in the previous section.

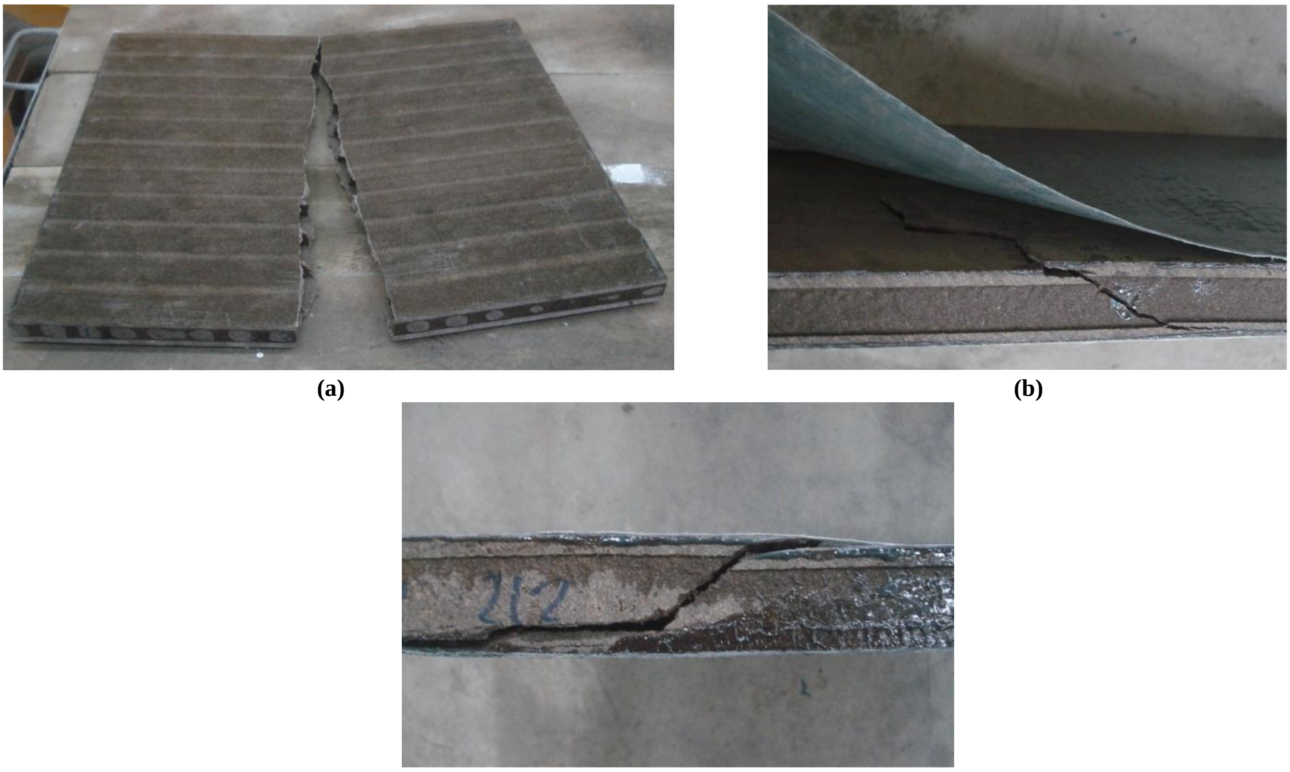

(a) (b) (c)

Fig. 22. Failure mode of specimens under flexural loads: (a) A0, (b) A1, and (c) A2.

By applying a point load to specimens A0 through A3, it was observed that in all cases, due to the hollow nature of the panels and the localized loading, the web directly beneath the applied load was unable to sustain the entire force because of its relatively low strength. Consequently, a cavity formed immediately under the load, leading to what is commonly referred to as punching shear failure. In Fig. 23a, the cracks formed beneath specimen P0 during loading are shown. As noted earlier, these cracks developed directly under the concentrated load. Fig. 23b presents specimen P2, in which the applied load exceeded the specimen’s capacity, leading to perforation. In Fig. 23c, the perforation observed in specimen P3 is illustrated; as can be seen, part of the GFRP in direct contact with the loading cylinder was torn due to excessive deformation following the occurrence of punching shear.

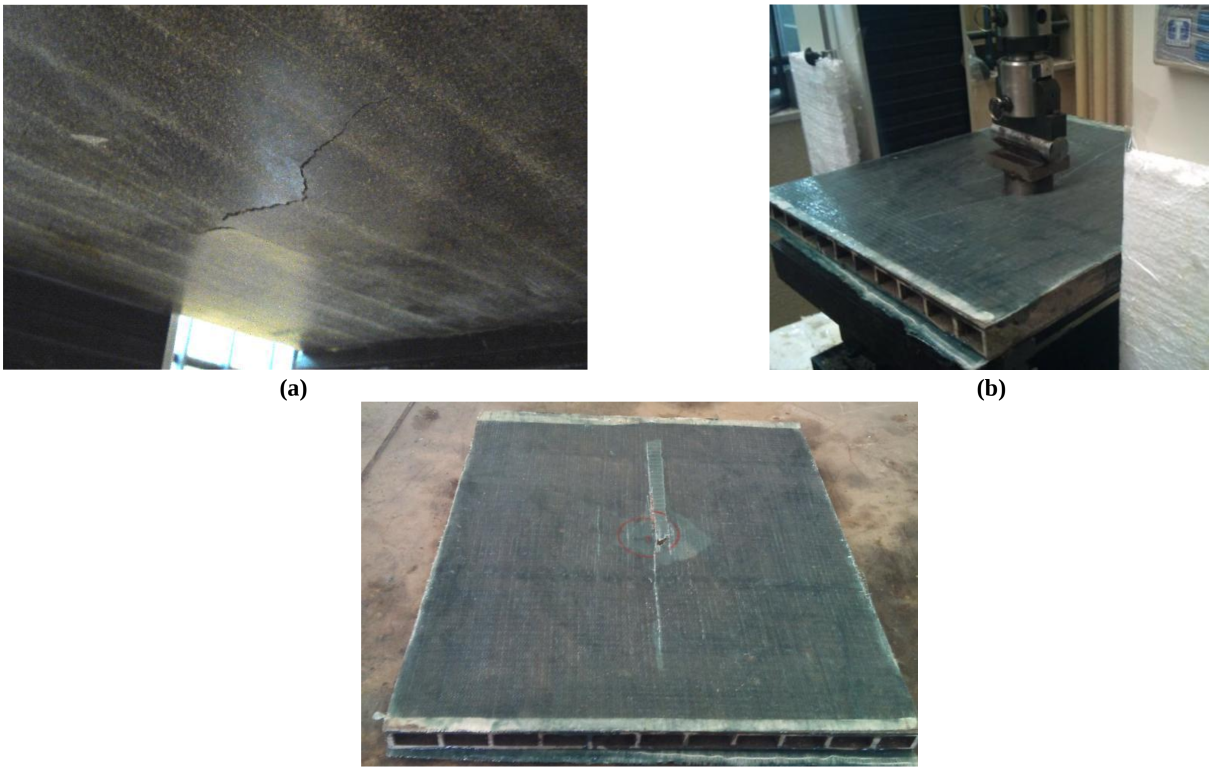
(a) (b)

(c)

Fig. 23. Failure mode of specimens under point loads: (a) P0, (b) P2, and (c) P3.

6.2. WPC uniaxial loading test

As described in the previous sections, uniaxial compression and tension tests were conducted to evaluate the mechanical behavior of the WPC. The results obtained from these tests are presented in Fig. 24.

As shown in Fig. 24, in addition to the stress–strain curves of the tested specimens, a dashed curve is presented, representing a fitted second-order polynomial. This curve was obtained by minimizing the error with respect to the experimental data. Specifically, if the stress–strain relationship is expressed as for compression and for tension, the corresponding values of A and were determined from this fitted curve and are summarized in Table 7.

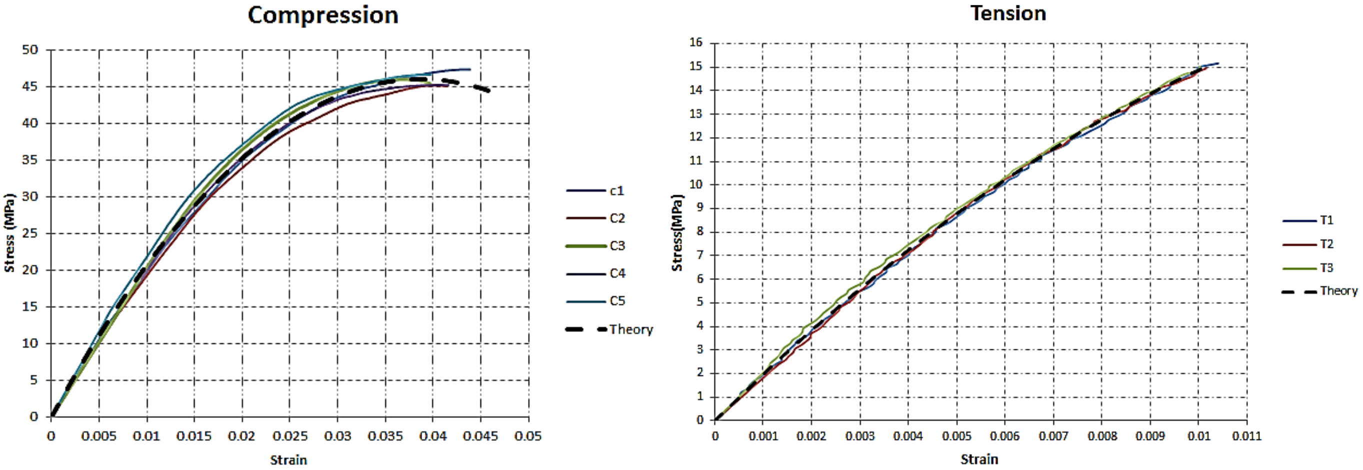

(a) (b)

Fig. 24. WPC uniaxial loading test; (a) compression, and (b) tension.

Table 7. The properties of WPC.

Tesion		Compression	
A	B	A'	B'
-18067.6	2377.059	-31660.8	2026.33

6.3. WPC linear loading test

The results of linear loading tests on specimens A0 through A3 are examined. The loading was applied up to the point of specimen failure. The corresponding experimental load-displacement curves for these tests are presented in Fig. 25.

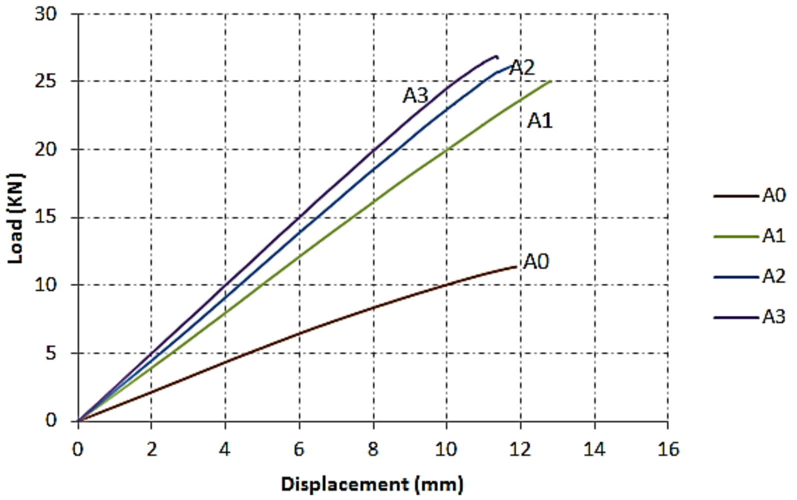

Fig. 25. Experimental load-deflection of WPC linear loading test.

As can be observed, the application of a single GFRP layer led to a significant enhancement in both the strength and stiffness of the panels, with the ultimate load increasing by 120% and stiffness by 84%. With the addition of an extra bottom layer in specimen A2, only an 8% increase in ultimate load was achieved compared to A1, while stiffness increased by 25%. The trend of strength improvement in specimen A3 reinforced with one top layer and three bottom layers was similar to that of A2, though at a much lower rate. Specifically, specimen A3 exhibited an 8% higher ultimate load and a 25% increase in stiffness relative to A2, as summarized in Table 8.

Table 8. Experimental results of WPC linear loading.

Specimen	Ultimate load (kN)	Percentage of changes (%)	Initial stiffness (N/mm)	Percentage of changes (%)	Final deformation (mm)
A0	11.371	-	1072.9	-	11.88
A1	25.045	120.3	1977.6	84.0	12.81
A2	27.979	138.5	2234.3	109.1	11.77
A3	26.877	136.4	2506.8	133.6	11.37

6.4. WPC point loading test

The results of the second series of tests on specimens A0 through A3, subjected to point loading, are presented in Fig. 26 and Table 9. To differentiate these specimens from the previous series tested under linear loading, they have been designated as P0 through P3.

As can be observed, the schematic results are similar to those of the linear loading case; however, quantitatively, there are notable differences, with both deformation and ultimate load being lower than in the previous series. In specimen P0, which had no GFRP face sheets, failure occurred under a load of approximately 600 kg. In contrast, specimen P1, reinforced with a single layer on both the top and bottom surfaces, failed under a load of 920 kg, representing nearly a 49% increase in load-bearing capacity.

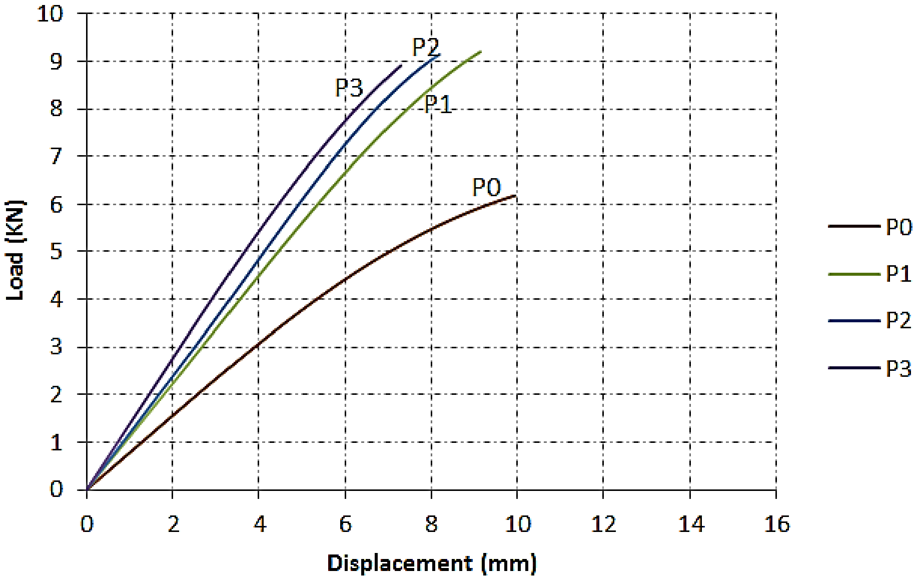

Fig. 26. Experimental load-deflection of WPC point loading test.

As shown in Fig.26, the load–deflection curves demonstrate an initially linear response followed by gradual stiffness degradation after yielding, indicating a ductile failure mechanism governed by the WPC core.

With the addition of more layers, the ultimate load did not increase significantly. This is attributed to the relative weakness of the web compared to the new face sheets: before the face sheets could effectively contribute, shear forces generated in the web beneath the point load caused localized failure in that region. Nevertheless, the added layers did influence the structural stiffness. For instance, in specimen P0, the initial stiffness was 777 N/mm, while the addition of one layer increased the stiffness by 43%. Adding another layer resulted in a further 10% increase, and in specimen P3 reinforced with one top layer and three bottom layers, the stiffness was 7% higher than that of specimen P0. According to Table 9, specimens reinforced with two GFRP layers exhibited approximately 18–22% higher ultimate load compared with unreinforced panels.

Table 9. Experimental results of WPC point loading.

Specimen	Ultimate load (kN)	Percentage of changes (%)	Initial stiffness (N/mm)	Percentage of changes (%)	Final deformation (mm)
P0	6.182	-	777.7	-	9.55
P1	9.200	48.8	1116.0	43.5	9.14
P2	9.444	47.9	1189.6	52.9	8.18
P3	8.912	44.1	1366.4	77.0	7.29

7. Theoretical results and discussion

7.1. WPC linear loading test

One of the approaches for determining the static behavior of sandwich panels is the beam theory method, which was explained in detail. Since the final derived equations were relatively complex and required step-by-step calculations, MATLAB software was employed to perform these computations. The results of these calculations for the four groups A0 to A3 are presented in Fig. 27 and Table 9.

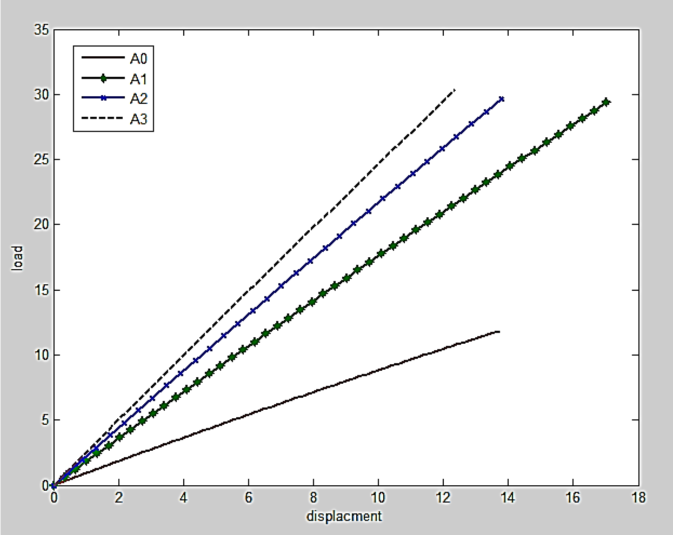

Fig. 27. Theoretical load-deflection of WPC linear loading test.

In specimen A1, the ultimate load increased by 148% and the stiffness by 95% compared to specimen A0. With the addition of an extra bottom layer in specimen A2, only a 3% increase in ultimate load was observed relative to A1, while the stiffness increased by 44%. The trend of strength enhancement in specimen A3 reinforced with one top layer and three bottom layers was similar to that of A2 but progressed at a slower rate. In particular, specimen A3 carried 6% more ultimate load and exhibited a 33% increase in stiffness compared to A2.

Table 10. Theoretical results of WPC linear loading.

Specimen	Ultimate load (kN)	Percentage of changes (%)	Initial stiffness (N/mm)	Percentage of changes (%)	Final deformation (mm)
A0	11.850	-	922.9	-	13.74
A1	28.380	147.9	1799.2	94.9	17.03
A2	29.633	150.2	2204.4	138.8	13.78
A3	30.363	156.2	2505.5	171.5	12.37

8. Numerical results and discussion

8.1. Validation of the numerical mode

To ensure the reliability and accuracy of the developed finite element (FE) model, a validation process was performed by comparing the numerical results with experimental and theoretical findings. The comparison focused on key response parameters, including the ultimate load, initial stiffness, and corresponding midspan deflection under both linear and point loading conditions. As summarized in Tables 12–14 and illustrated in Figures 32–35, the FE results showed a close agreement with the experimental data. For specimens subjected to linear loading, the difference between the experimental and numerical ultimate loads ranged from 2% to 9%, while the deviation in initial stiffness values was less than 6% for most specimens. For point-loaded specimens, the corresponding differences were within 2%–12%.

his level of consistency confirms that the finite element model accurately reproduces the mechanical behavior of the WPC–GFRP sandwich panels. The observed minor discrepancies are mainly due to experimental uncertainties, manufacturing imperfections, and simplifications in boundary condition modeling. Overall, the model demonstrates high predictive capability and can be reliably used for further parametric and optimization analyses of WPC–GFRP composite systems.

8.2. WPC linear loading test

In the finite element method, after creating the model, applying the load, and performing meshing as described in detail in the previous section, each specimen was analyzed in the software. Upon completion of the analysis, the deformation resulting from loading was displayed schematically by the software. Fig. 28 illustrates the deformation of specimen A0.

As shown in the figure, due to the linear nature of the applied loading, the maximum deformation also occurs linearly at the midspan of the panel. The load-displacement curves of specimens A0 through A3 are presented in Fig. 29, and the corresponding results are summarized in Table 11.

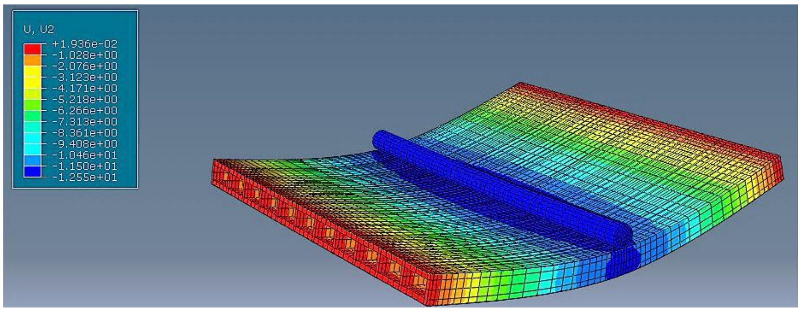

Fig. 28. Linear loading deformation of specimen A0.

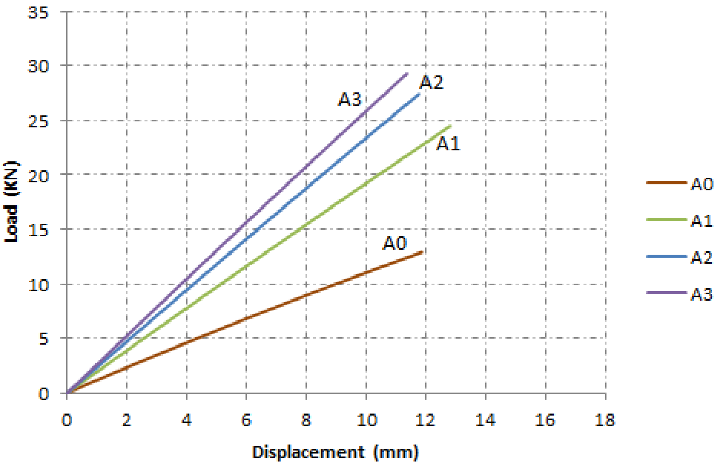

Fig. 29. Numerical load-deflection of WPC linear loading test.

Table 11. Numerical results of WPC linear loading.

Specimen	Ultimate load (kN)	Percentage of changes (%)	Initial stiffness (N/mm)	Percentage of changes (%)	Final deformation (mm)
A0	12.191	-	1287.20	-	11.86
A1	23.466	89.42	2028.79	65.18	12.81
A2	27.406	124.6	2246.66	98.83	11.77
A3	29.299	146.7	2633.13	126.4	11.26

8.3. WPC point loading test

Point loading was also investigated using the numerical method, with the specimens modeled in accordance with the experimental tests. The diagrams obtained from the finite element modeling are presented in Fig. 30. As can be seen, there is a good agreement between these curves and the experimental results, which will be further discussed in the following section. The numerical results obtained from this loading condition are fully presented in Table 11. Fig. 31 presents the schematic deformation of specimen

P2. As can be observed, the deformation at the midspan of the panel is significantly larger, and this type of loading results in the formation of a perforation at the center.

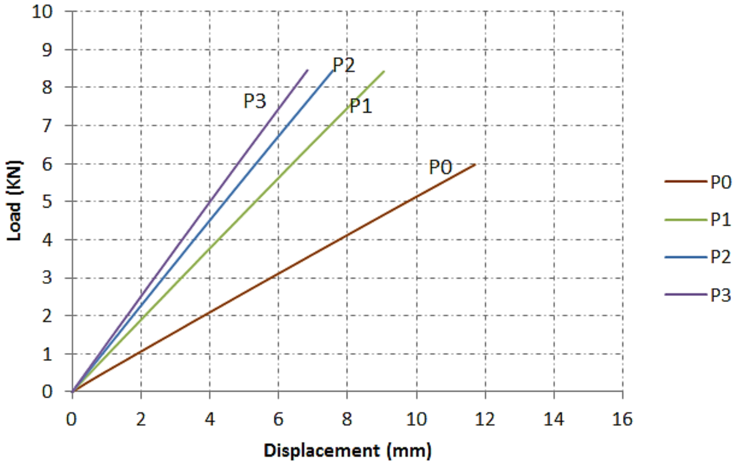

Fig. 30. Numerical load-deflection of WPC point loading test.

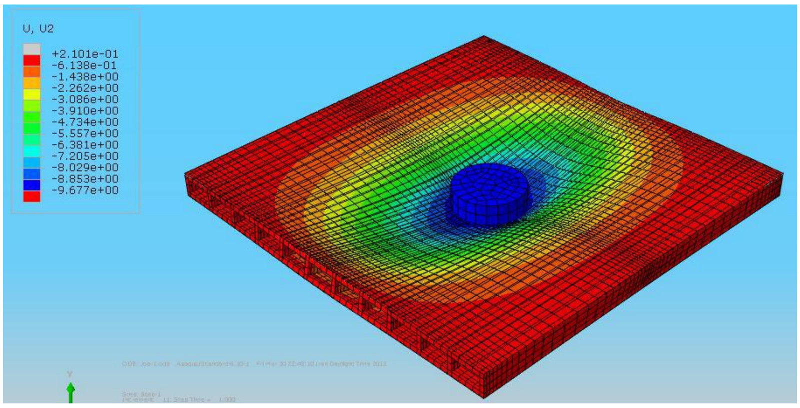

Fig. 31. Point loading deformation of specimen P2.

Table 12. Numerical results of WPC point loading.

Specimen	Ultimate load (kN)	Percentage of changes (%)	Initial stiffness (N/mm)	Percentage of changes (%)	Final deformation (mm)
P0	5.98	-	570.91	-	11.70
P1	8.43	41.02	990.28	73.46	9.05
P2	8.45	41.43	1170.44	105.01	5.57
P3	8.46	41.59	1290.69	126.07	6.83

As previously mentioned, the experimental loading was applied in the form of displacement control at a constant rate. To ensure that the modeling corresponded closely with the experimental procedure, the loading in ABAQUS was also applied in the form of displacement control. This displacement was continued until the shear stress in the WPC web reached its maximum value. For example, the shear stress distribution in specimen P3 along a cross-section at the midspan is shown in Fig. 31.

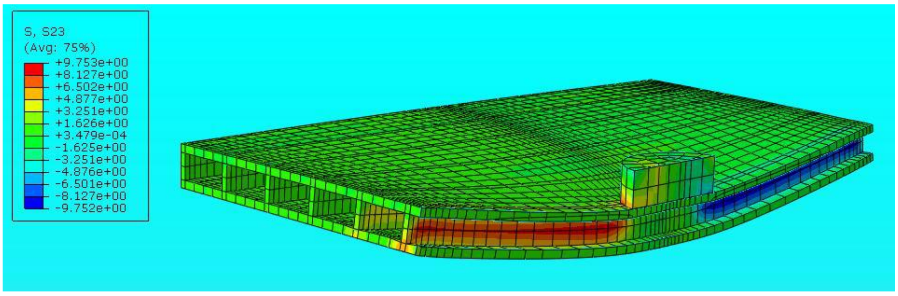

Fig. 32. Point loading deformation of specimen P3.

9. Comparison between experimental, theoretical, and numerical results in linear loading

To verify the accuracy of the theoretical and numerical methods employed in the modeling and analysis of the panels, the results for each specimen obtained from all three approaches were plotted together in a single diagram. These comparisons of initial stiffness and ultimate load are presented in Tables 13 and 14, respectively.

Table 13. Comparison of the initial stiffness of the WPC specimens under linear loading.

Specimen	Experimental (N/mm)	Theoretical (N/mm)	Error (%)	Numerical (N/mm)	Error (%)
A0	1139.18	905.23	20.54	1103.56	3.13
A1	2037.50	1760.55	13.36	1919.00	5.54
A2	2466.49	2168.60	12.10	2339.90	5.06
A3	2470.15	2466.70	12.10	2591.30	4.90

Table 14. Comparison of the ultimate load of the WPC specimens under linear loading.

Specimen	Experimental (kN/mm)	Theoretical (kN/mm)	Error (%)	Numerical (kN/mm)	Error (%)
A0	11.38	11.15	1.95	12.91	13.51
A1	25.05	29.38	17.27	24.46	2.34
A2	25.80	29.64	14.91	27.46	6.21
A3	26.88	30.26	12.97	29.29	8.98

As shown in Fig. 33, for specimen A0, the numerical method exhibits good accuracy, with an error of less than 4% in the stiffness parameter (i.e., the slope of the load-displacement curve) compared to the experimental results. In contrast, the theoretical method shows an error of nearly 20%, which can be attributed to the neglect of Poisson's ratio in the beam theory formulation.

For specimen A1, with the addition of one GFRP layer on both the top and bottom surfaces, the stiffness of the beam increased, and the panel's behavior became more influenced by the reinforcing layers. Since GFRP exhibits unidirectional behavior, and beam theory remains applicable with increasing width, the error in the slope of the curve decreased from 20% to 13.36%. A similar trend is observed with the numerical method, where the error was reduced to less than 6%.

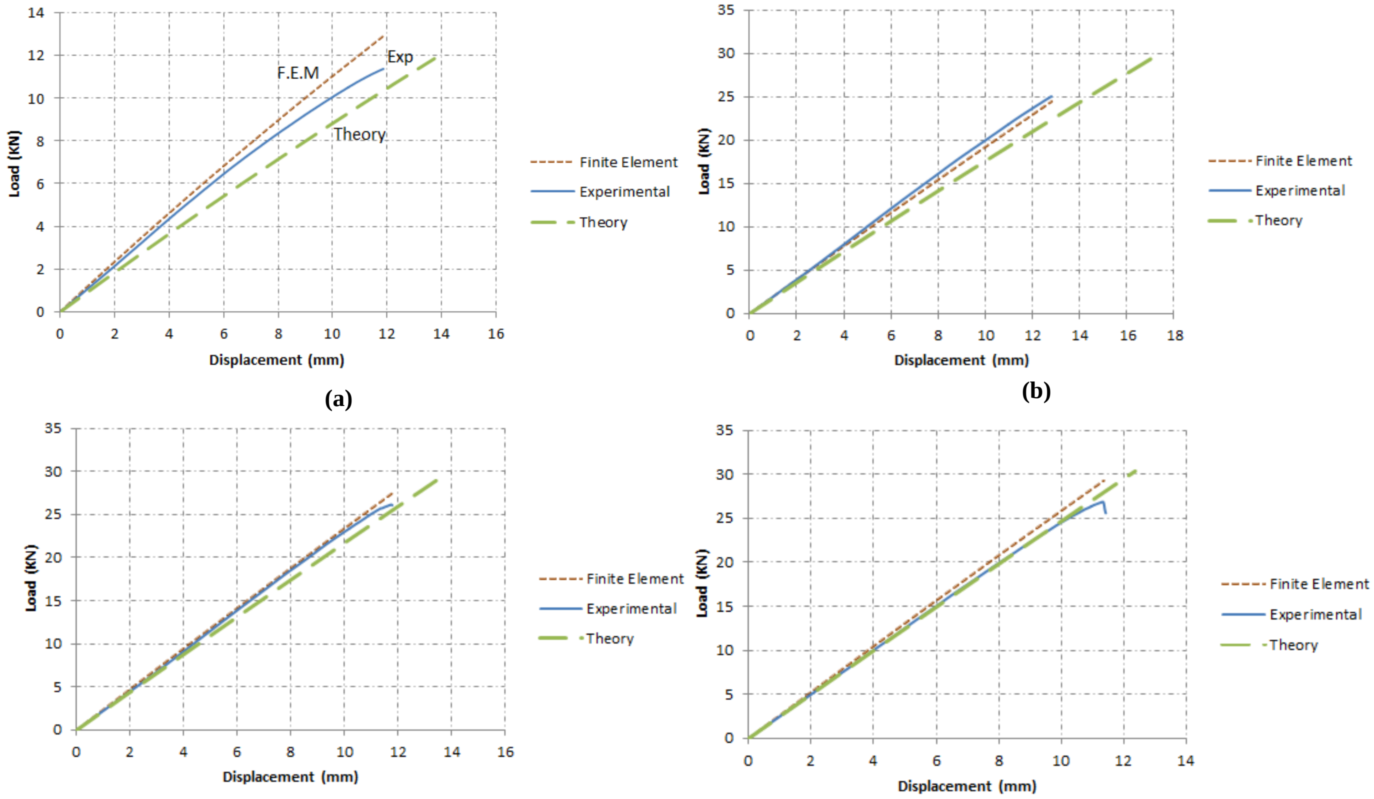

(a) (b)

(c) (d)

Fig. 33. Comparative linear loading load-displacement curve; (a) A0, (b) A1, (c) A2, and (c) A3.

For specimen A2, as shown in Fig. 33, the theoretical method more closely matches the experimental curve. This can be attributed to the increased stiffness of the panel due to the additional reinforcing layers, which, as previously noted, exhibit good compatibility with beam theory. The numerical curve, similar to the previous specimen, also aligns well with the experimental data, with an error of about 5%. However, as indicated in Table 13, which compares the ultimate loads of the panels, the theoretical and numerical methods predict approximately 30% and 7% higher ultimate loads, respectively, than those obtained experimentally. This discrepancy can be explained by the lack of homogeneity in the panel core, which caused premature failure of the specimen.

For specimen A3, the agreement between the curves is even stronger than before, with the error of the theoretical method reduced to less than 1% and that of the numerical method to below 5%. Moreover, the ultimate load obtained from the numerical method is only 9% higher than the experimental value, while the error in the theoretical method decreased by 2% compared to specimen A2.

A separate comparison between the theoretical and numerical methods provides a clearer understanding of the differences between these two curves. As shown in Figs. 34 and 35, in general, the specimens analyzed by the numerical method exhibit higher stiffness.

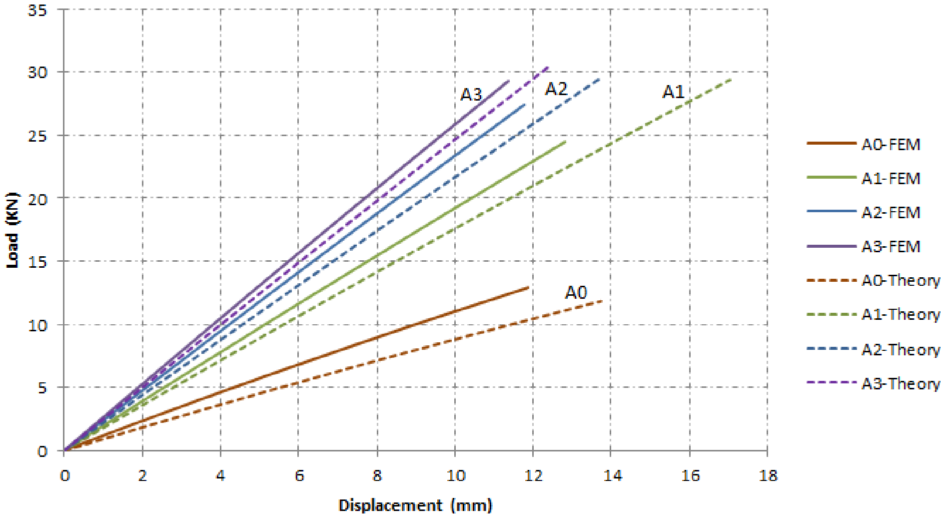

Fig. 34. Comparison between results from theoretical and numerical methods in linear loading.

Moreover, as the number of layers increases, the curves converge more closely. This convergence can be attributed to the dominant role of the GFRP layers and the good compatibility of the beam theory model with the actual behavior of the panels.

The observed reduction in the rate of strength increase with successive GFRP layers can be explained by the mechanics of stress transfer and interfacial behavior between the composite layers. As the number of GFRP sheets increases, the stiffness contrast between the outer reinforcement and the WPC core becomes more pronounced. Because the epoxy adhesive possesses limited shear stiffness, only part of the tensile force developed in the outer GFRP is effectively transmitted to the substrate, resulting in stress transfer inefficiency. Furthermore, the mismatch in strain compatibility between the relatively brittle GFRP and the more ductile WPC induces localized debonding and micro-slip at the interface before global failure, as confirmed by the gradual separation observed in several specimens. The neutral axis also shifts toward the tension side as reinforcement thickness increases, reducing the lever arm efficiency and producing diminishing incremental gains in flexural capacity. These combined effects explain why the addition of the third GFRP layer (specimen A3) provided only a modest increase in ultimate load compared with the second layer (specimen A2), consistent with the nonlinear stiffness trends predicted numerically.

Although all specimens were prepared and tested under carefully controlled conditions, several factors may have contributed to minor variations among the results. The most significant source of experimental uncertainty is associated with bonding quality between the GFRP layers and the WPC substrate. Despite surface grinding and thorough cleaning, small variations in surface roughness and epoxy thickness may have led to localized stress concentrations and partial debonding in some specimens. Another potential source of variation arises from the inhomogeneity of the WPC material, where local differences in the wood–plastic fiber ratio and density could influence stiffness and failure strain. Environmental factors such as temperature and humidity during the 7–10 day curing period may also have affected adhesive hardening and bond strength. Additionally, instrumentation errors including load cell precision (±1%) and displacement transducer tolerance (±0.5%) introduce small but unavoidable measurement deviations. Considering these factors, the discrepancies between the experimental, theoretical, and numerical results (generally within 10%) fall well within the expected range of uncertainty, confirming the overall reliability of the experimental data.

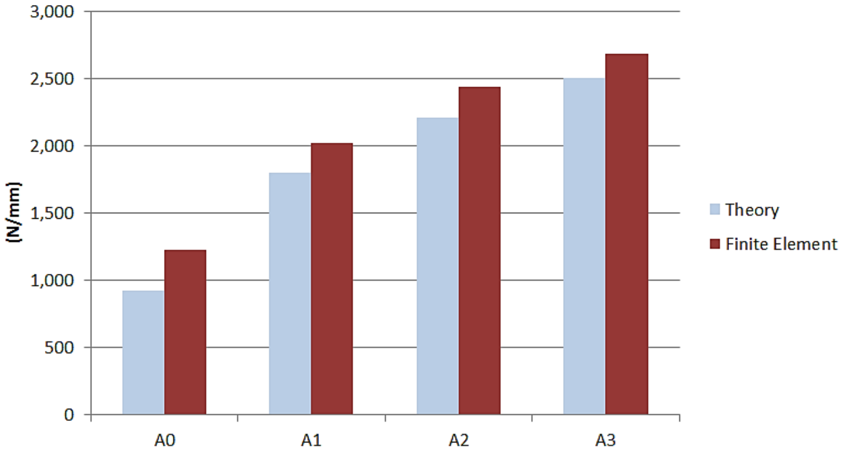

Fig. 35. Comparison of the initial stiffness of samples from theoretical and numerical methods under linear loading.

10. Comparison between experimental and numerical results in point loading

Similar to the linear loading case, a comparison is made between the point loading experimental curves and those obtained from the numerical method. Overall, the results of this comparison for the initial stiffness of the specimens are presented in Table 15.

Table 15. Comparison of the initial stiffness of the WPC specimens under point loading.

Specimen	Experimental (N/mm)	Numerical (N/mm)	Error (%)
P0	777.7	570.91	26.59
P1	1116.0	990.28	11.27
P2	1189.6	1170.44	1.61
P3	1366.4	1290.69	6.23

The comparative point load-displacement curve for specimens obtained from the numerical and experimental methods is shown in Fig. 36. As seen from the curve and the corresponding results, the ultimate load of the P0 specimen exhibits less agreement compared to the other curves, with an error of approximately 26%. This discrepancy remains nearly constant throughout the curve. For specimen P1, the difference is reduced, with the error decreasing by about 15%. Furthermore, the ultimate load shows a smaller percentage error, with only a 9% difference between the numerical and experimental curves.

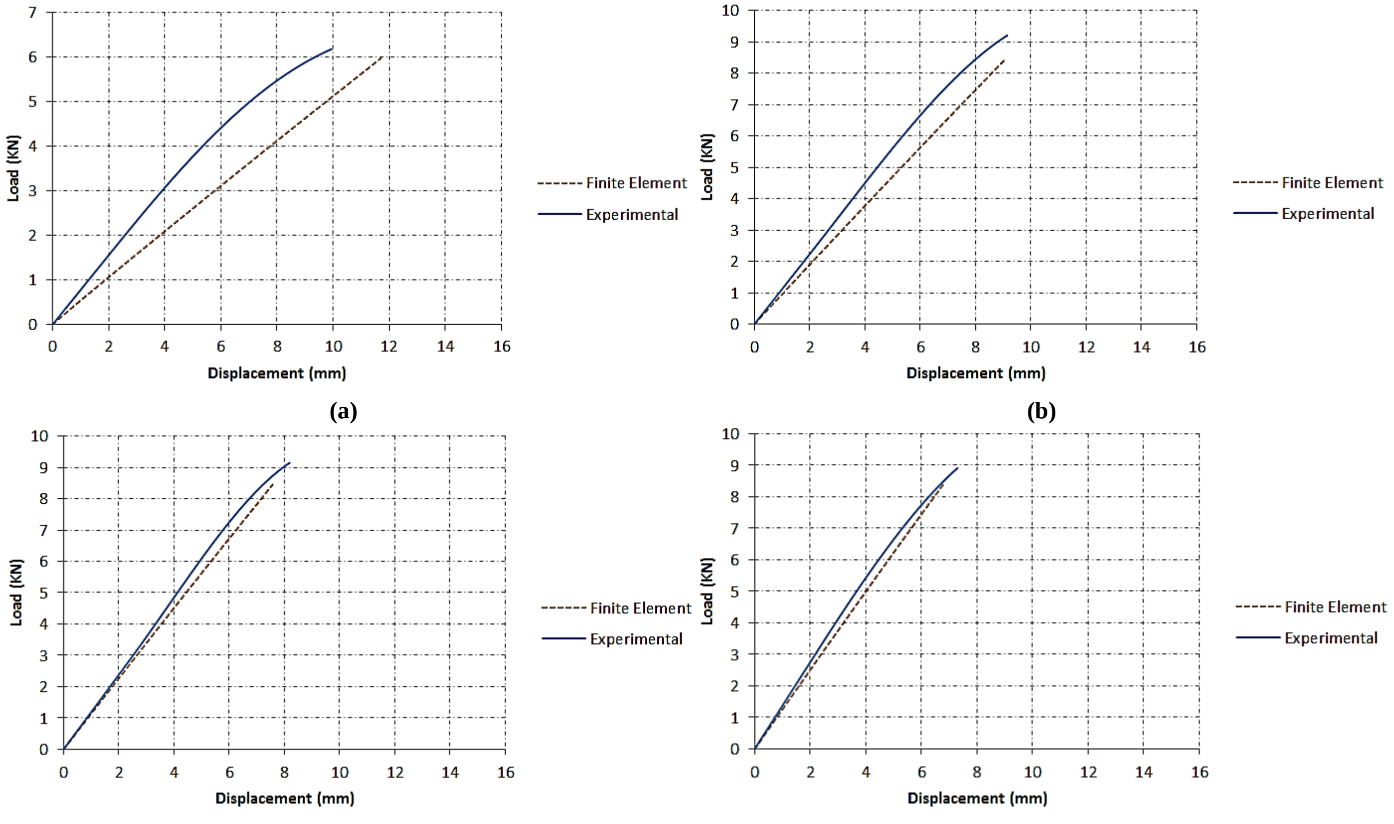

(a) (b)

(c) (d)

Fig. 36. Comparative point loading load-displacement curve; (a) P0, (b) P1, (c) P2, and (c) P3.

In specimen P2, the discrepancy reached its minimum, with the initial stiffness obtained from the numerical method differing by only 1.6% from the experimental result. This small difference appears at the beginning of the curve, while a slight deviation develops in the middle section; nevertheless, the two curves remain close overall. In specimen P3, a similar trend to P2 is observed, with only minor differences between the two curves. However, unlike P2, the initial slope of the P3 curve shows a 6% deviation, which decreases as the curve progresses. Such minor discrepancies can be attributed to experimental errors.

In general, specimens subjected to point loading exhibited greater differences between the numerical and experimental results compared to those under linear loading. This can be explained by the lack of uniformity in the WPC dimensions, which has a more pronounced effect in point-loaded specimens. Nevertheless, as observed, there is an overall good agreement between the two methods.

11. Conclusions

In this study, WPC-GFRP specimens with different numbers of reinforcing layers were tested under two types of loading. For the theoretical analysis, beam theory and the flexural surface method were employed. In addition, the numerical method was used for a better comparison of results. The main findings of the present research can be summarized as follows:

- The use of reinforcing layers in WPC and the creation of sandwich panels led to a significant increase in structural stiffness. With just one GFRP layer of 0.12 mm thickness, the stiffness increased by 80%.
- The formation of sandwich panels also resulted in a considerable increase in the ultimate load, such that the addition of a single GFRP reinforcing layer increased the ultimate load by 120%.
- Increasing the number of reinforcing layers further enhanced the panel stiffness, but the rate of stiffness improvement diminished with each additional layer.

- Adding more reinforcing layers did not result in a substantial increase in ultimate load. This is due to the relative weakness of the core compared to the face sheets; the core (WPC) experienced shear failure before the additional layers could become fully effective. Therefore, applying more than one GFRP layer in WPC-GFRP sandwich panels is not economically justifiable.
- Linear loading produced better results than point loading, with the structures sustaining higher ultimate loads. This difference is explained by the hollow nature of sandwich panels, which makes them susceptible to punching shear under point loading.
- The displacement of plates with two free edges under linear loading perpendicular to those edges can be reasonably calculated using beam theory. If the aspect ratio of the plate (length-to-width) is infinite, the error between the two methods is less than 1%. For a plate with a length-to-width ratio of 1, the error increases to about 9%.
- In comparing experimental and theoretical results for the unreinforced specimen, a 20% difference was observed in the initial stiffness. However, this difference decreased in the reinforced specimens; for example, in specimen A3 with three reinforcing layers, the theoretical result differed from the experimental result by less than 1%. This is because, with the addition of layers and the unidirectional behavior of FRP, the stiffness of the panels becomes dominated by the FRP, and their behavior approaches that of beams, making beam theory predictions more accurate.
- In the FEM, the results for the unreinforced specimen were much closer to the experimental data, since the effect of Poisson’s ratio of the WPC, which is neglected in beam theory, was accounted for in FEM.
- In FEM, the stiffness of the specimens was slightly higher than the experimental results, which can be attributed to experimental errors. For instance, lack of homogeneity in the specimens and the presence of air voids during fabrication may have caused microscopic defects in the material, leading to reduced stiffness under loading.

12. Recommendations for future research

As demonstrated in this study, the use of theoretical and numerical methods can provide results close to the desired outcomes without the expense of experimental testing. Considering this advantage, along with the higher accuracy and speed of software-based modeling compared to experimental approaches, the use of numerical simulation is recommended. For future research, the following topics can be addressed through modeling and numerical analysis, to facilitate their practical implementation based on the findings:

- Investigation of the dynamic behavior of WPC-GFRP sandwich panels.
- Evaluation of the effect of different grooves on the ultimate strength of WPC-GFRP panels.
- Theoretical and experimental study of the flexural behavior of WPC-GFRP panels with varying length-to-width ratios.
- Examination of methods to improve the shear strength of WPC specimens.
- Determination of the optimum WPC cross-section dimensions in sandwich panels.
- Selection of the most effective reinforcing layer for use in WPC-GFRP sandwich panels.
- Optimization of GFRP thickness for application in WPC-GFRP sandwich panels.

Statements & Declarations

Author contributions

Amin Norouzi: Conceptualization, Investigation, Methodology, Formal analysis, Resources, Writing - Original Draft, Writing - Review & Editing.

Morteza Naghipour: Conceptualization, Methodology, Formal analysis, Project administration, Supervision, Writing - Review & Editing.

Funding

The authors received no financial support for the research, authorship, and/or publication of this article.

Data availability

The data presented in this study will be available on interested request from the corresponding author.

Declarations

The authors declare no conflict of interest.

References

[1] Friedrich, D. Thermoplastic moulding of Wood-Polymer Composites (WPC): A review on physical and mechanical behaviour under hot-pressing technique. Composite Structures, 2021; 262: 113649. doi:10.1016/j.compstruct.2021.113649.

[2] Naghipour, M., Arefi, S. L., Nematzadeh, M. Performance of longitudinal grooves to prevent debonding of GFRP sheets used for the reinforcement of WPC beams. European Journal of Environmental and Civil Engineering, 2013; 17: 761-776. doi:10.1080/19648189.2013.815136.

[3] Gardner, D. J., Han, Y., Wang, L. Wood–Plastic Composite Technology. Current Forestry Reports, 2015; 1: 139-150. doi:10.1007/s40725-015-0016-6.

[4] Naghipour, M., Nematzadeh, M., Yahyazadeh, Q. Analytical and experimental study on flexural performance of WPC–FRP beams. Construction and Building Materials, 2011; 25: 829-837. doi:10.1016/j.conbuildmat.2010.06.104.

[5] Wechsler, A., Hiziroglu, S. Some of the properties of wood–plastic composites. Building and Environment, 2007; 42: 2637-2644. doi:10.1016/j.buildenv.2006.06.018.

[6] Chini, M., Arefi Lale, S., Zolfani Hashemkhani, S., Ustinovicius, L. Choosing a proper method for strengthening WPC beams with grooving method using SWARA-EDAS. Archives of Civil Engineering, 2018; 64: 161-174. doi:10.2478/ace-2018-0050.

[7] Li, Y.-F., Tsai, M.-J., Wei, T.-F., Wang, W.-C. A study on wood beams strengthened by FRP composite materials. Construction and Building Materials, 2014; 62: 118-125. doi:10.1016/j.conbuildmat.2014.03.036.

[8] Lale Arefi, S., Naghipour, M., Turskis, Z., Nematzadeh, M. Evaluation of grooving method to postpone debonding of FRP laminates in WPC-FRP beams. Journal of Civil Engineering and Management, 2014; 20: 237-246. doi:10.3846/13923730.2013.878379.

[9] Zolfaghari, A., Behravesh, A. H., Adli, A. Continuous glass fiber reinforced wood plastic composite in extrusion process: Mechanical properties. Materials & Design, 2013; 51: 701-708. doi:10.1016/j.matdes.2013.04.082.

[10] Behravesh, A., Zohdi Aghdam, A., Soury, E. Experimental investigation of injection molding of wood/plastics composites. Journal of reinforced plastics and composites, 2010; 29: 456-465. doi:10.1177/0731684408099406.

[11] Li, Y.-F., Xie, Y.-M., Tsai, M.-J. Enhancement of the flexural performance of retrofitted wood beams using CFRP composite sheets. Construction and Building Materials, 2009; 23: 411-422. doi:10.1016/j.conbuildmat.2007.11.005.

[12] Plevris, N., Triantafillou Thanasis, C. FRP-Reinforced Wood as Structural Material. Journal of Materials in Civil Engineering, 1992; 4: 300-317. doi:10.1061/(ASCE)0899-1561(1992)4:3(300).

[13] Triantafillou Thanasis, C., Deskovic, N. Prestressed FRP Sheets as External Reinforcement of Wood Members. Journal of Structural Engineering, 1992; 118: 1270-1284. doi:10.1061/(ASCE)0733-9445(1992)118:5(1270).

[14] Naghipour, M., Taheri, F., Zou, G. P. Evaluation of Vibration Damping of Glass-Reinforced-Polymer-Reinforced Glulam Composite Beams. Journal of Structural Engineering, 2005; 131: 1044-1050. doi:10.1061/(ASCE)0733-9445(2005)131:7(1044).

[15] Adhikary, K. B., Pang, S., Staiger, M. P. Dimensional stability and mechanical behaviour of wood–plastic composites based on recycled and virgin high-density polyethylene (HDPE). Composites Part B: Engineering, 2008; 39: 807-815. doi:10.1016/j.compositesb.2007.10.005.

[16] Wang, K., Xu, X., Huo, R., Fang, H., Chen, X. Flexural reinforcement of wood plastic composite panels by bonding glass fiber reinforced polymer sheets and embedding bars. Polymer Composites, 2024; 45: 14595-14607. doi:10.1002/pc.28784.

[17] Wang, K., Yu, C., Liu, W., Huo, R., Fang, H., Chen, X. Study on flexural property of glass fiber-reinforced polymer reinforced wood–plastic composite panels. Wood Material Science & Engineering, 2025; 20: 478-487. doi:10.1080/17480272.2024.2355554.

[18] Jian, B., Mohrmann, S., Li, H., Li, Y., Ashraf, M., Zhou, J., Zheng, X. A Review on Flexural Properties of Wood-Plastic Composites. Polymers, 2022; 14: 3942. doi:10.3390/polym14193942.

[19] Hamed, E., Negru, D., Yalda, R. Structural Performance of Precast Concrete Sandwich Panels Made with FRP Vierendeel Truss–Like Connectors. Journal of Composites for Construction, 2022; 26: 04022027. doi:10.1061/(ASCE)CC.1943-5614.0001215.

[20] Huang, J.-Q., Dai, J.-G. Flexural performance of precast geopolymer concrete sandwich panel enabled by FRP connector. Composite Structures, 2020; 248: 112563. doi:10.1016/j.compstruct.2020.112563.

[21] ASTM International. ASTM D695: Standard test method for compressive properties of rigid plastics. West Conshohocken (PA): 1996. doi:10.1520/D0695-23.

[22] ASTM International. ASTM D638: Standard test method for tensile properties of plastics. West Conshohocken (PA): 2003. doi:10.1520/D0638-14.